2023

Investigation of Endothelial Mechanics on Primary Cell Functions: Endothelium Permeability and Wound Healing

Sean Beverung
University of Central Florida

INVESTIGATION OF ENDOTHELIAL MECHANICS ON PRIMARY CELL FUNCTIONS: ENDOTHELIUM PERMEABILITY AND WOUND-HEALING.

by

SEAN BEVERUNG

BS, UNIVERSTY OF CENTRAL FLORIDA, 2017
MS, UNIVERSITY OF CENTRAL FLORIDA, 2020

A dissertation submitted in partial fulfillment of the requirements
for the degree of Doctor of Philosophy
in the Department of Mechanical and Aerospace Engineering
in the College of Engineering and Computer Science
at the University of Central Florida
Orlando, Florida

Spring Term
2023

Major Professor: Robert L. Steward Jr

ABSTRACT

The endothelium composes the inner lining of blood vessels, the heart, and lymphatic vessels. Within the cardiovascular system, it is an extremely important structure, aiding in the regulation of blood pressure with the vascular tone, recruiting immune response, regulating the transfer of material in and out of the bloodstream, and the creation of new blood vessels through angiogenesis. The endothelium is composed entirely of endothelial cells. These cells lay in a flat squamous formation and are in direct contact with blood and aid in the regulation and transfer of material in and out of the bloodstream via active and passive transport. Passive transport is regulated with cell-cell junctions between the endothelial cells, otherwise known as intercellular junctions, is the topic of interest in our first study. One cell-cell junction, adherens junctions are connected to the cytoskeleton of actin filaments. These actin filaments play an important role in the cell's ability to generate force through the contraction of the actin-myosin complex creating tension in the filaments. Because of the direct link between these two structures, there is a belief that there is a connection between the permeability of the endothelium and the cellular forces produced by the actin cytoskeleton. Also, other cell-cell junctions, gap junctions, and tight junctions have shown that when disrupted endothelial permeability increases. These junctions' relation between function and cell mechanics is not as well-known. Our goal is to determine if disruption of these junctions causes a similar stress environment as disruption of adherens junctions with the use of traction force microscopy and monolayer stress microscopy. The endothelium also plays an important role in the process of wound-healing. We look the endothelial cells role in wound-healing process as part of our second study. When an injury occurs and there is damaged tissue with inadequate oxygenation endothelial cells migrate into

the wound space and begin the process of angiogenesis forming new blood vessels to support other cells in the process of wound-healing and providing oxygen to repair tissue. This process is so important that diseases that impede it can cause chronic wounds. To improve wound-healing rates, magnetic therapies have been looked at to stimulate the wound area and promote wound-healing. It is believed that cells are receptive to electrical and magnetic stimulation due to their ion-based communication methods. Magnetic field studies have shown promise in animal models. But contradictory results between different wound types and animal models leads us to look into an in-vitro human model to test the therapies potential effectiveness. To get a better idea of how magnetic therapy may affect human patients, we use human endothelial cells in an in-vitro scratch test study under several strength magnetic fields to determine if the therapies show any promise. Another therapy that shows promise is electrical stimulation. Studies show that the migration of single endothelial cells can be controlled using a voltage potential in-vitro. And in-vivo studies show promise in improving wound-healing times with diabetic ulcerations. To see if this improvement is potentially due to a collective migration response from the endothelial cells a similar set of scratch test in-vitro studies were conducted to see if endothelial wound-healing times improved under electrical stimulation. To determine the effectiveness of magnetic and electrical stimulations effect on wound-healing we look at the wound closure rate and average cell velocity of wounds created in these in-vitro models. Electrical stimulation has also shown promise as a wound-healing therapy with improvements in wound-healing for diabetic ulcers. Because of this improved wound-healing response from this therapy, we wish to look to see if endothelial cells are responsible for the improved wound-healing response. For electrical stimulation, a similar set of scratch tests were performed under a low voltage gradient

to determine if collective cell migration and endothelial wound-healing were affected by electrical stimulation.

ACKNOWLEDGMENTS

Thanks to Jovani Gutierrez, Hollie Sandler, Brad Moony, Anay Shah, Todd Condon Jr., and Jingwen Wu for their aid during the experimental setup and data processing. Thanks to Vignesh Balachandar and Mydul Islam for their aid in coding. Thanks to Gregory Alley for the use of his tangent field galvanometers.

My gratitude goes to Dr. Robert Steward Jr. for his years of support. Lending me his time, expertise, and use of his lab over the years. To whom without all of this would not be possible.

And thanks to Dr. Olusegun Ilegbusi, Dr. Hasan Mansy, and Dr. Manish Gupta for sitting on my dissertation committee.

This work was funded by the National Heart, Lung, And Blood Institute of the National Institute of Health under the award K25HL132098, the National Science Foundation CAREER Award under Grant No. 2045750, and the University of Central Florida start-up funds.

TABLE OF CONTENTS

LIST OF FIGURES

LIST OF TABLES

CHAPTER ONE: INTRODUCTION

Endothelial cells line the interior of blood and lymphatic vessels forming a semipermeable membrane that regulates the flow of materials into and out of the cardiovascular system. This permeability is maintained by cell-cell junctions [1], [2]. Tight and Adherens cell-cell junctions form a barrier by bonding two different cell walls together so material cannot pass between them[3], [4]. Several enzymes, enzyme inhibitors, hormones, and drugs can influence this permeability via interacting with these cell-cell bonds [5]–[8]. Cardiovascular diseases can also influence the permeability of the endothelium leading to endothelial dysfunction. Examples of such diseases are systemic capillary *leak syndrome* and diabetic retinopathy[9], [10]. Other non-cardiovascular diseases such as Covid-19 can damage the endothelium[11]. Being able to measure permeability is an important part of being able to determine if endothelial disruption has occurred. For this XPerT permeability analysis was selected to measure paracellular permeability with florescent avidin. Cell-Cell Junctions also allow for the transfer of forces between cells. The force interactions between endothelial cells are believed to be an important part of regulating permeability. Putting tension on adherens cell-cell junction is one of the ways endothelial cells increase permeability[8]. Because of this interconnected nature of cellular forces and permeability a method to measure cellular mechanical forces is needed. Traction Force microscopy and Intercellular Stress Microscopy are two tools that allow for the measurement of the forces exerted by cells on their surroundings[12]. Discerning how different forms of endothelial disruption is the first objective of my dissertation.

Our second endothelial function of interest is wound-healing. Endothelial cells play an important role in the wound-healing process and better understanding how to control their migration can play a role in the development of medical therapies. Improved healing rates provide faster recovery times for patients and reduce the risk of infection and can provide better patient outcomes. One therapy that has been studied with mixed effectiveness is electromagnetic stimulation of the wounded area. My second dissertation goal is to look at magnetic and electrical stimulation therapies and investigate their effects on endothelial cells to determine their efficacy [13], [14]. For these wound closure experiments endothelial cells are used due to the vital role they play in the process of wound-healing through angiogenesis. Angiogenesis is the process where endothelial cells form new blood vessels. Angiogenesis is a limiting factor for wound-healing as other cells need the revascularization of damaged tissue. This is because the cells that create granular tissue in the wound-healing process require a sustained oxygen supply provided by blood flow [15], [16]. An important step of angiogenesis is the proliferation and migration of endothelial cells into damaged tissue areas. To improve healing outcomes, the proliferation and migration of endothelial cells are used as an indicator for the rate of wound-healing. A scratch test measures the collective cell migration in two dimensions of an invitro wound. Scratch tests are common tests used to measure wound-healing[17].

CHAPTER TWO: LITERATURE REVIEW

Mechanosensing

One of the principles of cell mechanics is the ability of cells to exert and react to forces exerted upon them. Cells can exert forces through the contraction of the actomyosin complex. This contractile force plays an important role in movement and other functions of anchorage dependent animal cells. This actin is attached to mechanosensing proteins such as talin and vinculin at both cell-substrate and cell-cell junctions [3], [12], [18]–[22]. These proteins, when placed under tension, cause conformational changes that promote the binding and polymerization of more actomyosin. This adaptive cytoskeleton is important for both barrier function and cell migration[23]–[27]. Together a cell can both generate and sense the forces it generates, along with forces generated by neighboring cells. Force generation and mechanosensing play an important role in several important cellular functions including cell migration, muscular force generation, communication through intercellular stresses, and barrier function[25]–[29]. Cell-substrate and cell-cell junctions are how internal cellular forces are transferred to the cells' surroundings via direct bonds via transmembrane proteins that connect the interior and exterior cellular space and allow force transfer though the cell wall. As the cell puts tension on its actin filaments it can exert forces on to substrate that causes its deformation. The forces exerted by cells can be determined by these deformations to the substrate and can be measured using a method called Traction force microscopy (TFM)[30]. The mechanics of two cellular functions have been the chosen focus of our studies as they contribute to two of the major functions of Endothelial cells; permeability and wound-healing (Figure 1).

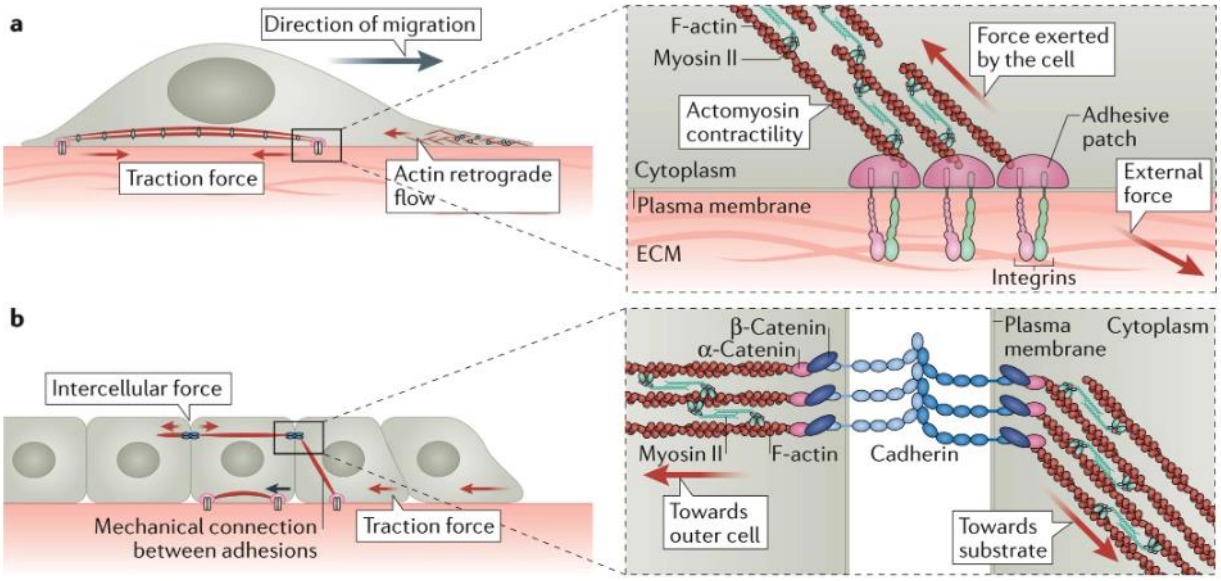

Figure 1: *a) Tractions exerted on opposed by cell-substrate as part of cell migration detected through integrins b) Transfer of tractions to intercellular forces through the cytoskeleton and cell-cell junctions*[23]

Endothelial Mechanics and Endothelial Permeability

One of the primary roles of endothelial cells is to act as a semipermeable barrier. The barrier functions of the cells are facilitated by the network of cell-cell junctions that the endothelial cells create with one another. Two junction types are believed to contribute to the barrier function of endothelial cells. The tight junctions and adherens junctions[2], [4], [31], [32]. There is one other type of cell-cell junction that exists between endothelial cells' gap junctions. Gap junctions allow for the transport of small molecules and ions between cells. Through the transfer of these signaling molecules and ions, the endothelial cells can communicate with one another. There is also some evidence that gap junctions may also support some structural functions and allow the transfer of forces between cells[4], [33]–[36]. One of the unique and most fundamental junctional protein types for endothelial cells is vascular endothelial cadherin (VE-cadherin). This is one of the essential proteins in adherens junctions between endothelial cells. VE-cadherin is

often associated with cell mechanics and with barrier function as it is linked to the actin cytoskeleton with mechanosensing molecules and had been shown to reorganize into clusters under the tension from the actin-myosin contraction demonstrating the interconnected nature of cell permeability and cellular mechanics [37]–[40]. Another characterizing binding protein is Claudin-5 which helps form tight junctions[37]–[40]. Claudin-5 is instrumental in the extremely selective blood-brain barrier were it fomes a closely knit arrangement of junctions to inhibit the passage of materials theses junctions are also linked to the actin cytoskeleton[1], [12], [41], [42].

To target the cell-cell junctions, treatments were selected that have been shown to increase endothelial permeability. These treatments are 2,5- dihydroxychalcone (Chalcone), Thapsigargin, Histamine, and Thrombin. Chalcone influences gap junctions by rapidly down-regulating Connexin 43 (Cx43). via its phosphorylation[5]. Histamine disrupts barrier function by rearranging adherens junctions with the activation of RhoA by increasing intracellular calcium levels. This is done as RhoA activates and causes the phosphorylation of light myosin putting tension on adherens junctions. Thapsigargin affects VE-cadherin junctions by increasing intercellular calcium levels and inducing the activation of PKCα causing the disassembly of VE-cadherin[7]. Thrombin disrupts tight junctions by affecting Claudin-5. This is believed to be through the activation of protease-activated receptor one [6]. Chalcone at a dosage of .2 and 2μg/ml have shown in the past that disruption of the gap junctions can cause changes in the mechanical environment of the endothelium with a reduction of tractions and intercellular stresses 2 μg/ml but an increased cell-substrate traction and average normal intercellular stresses with a reduction in maximum intercellular shear stresses[43]. Histamine disruption of the endothelium through tension on adherens junctions has been observed under several concentrations and had been associated

with increased cell-substrate tractions and intercellular average normal cell-cell stresses [8], [44], [45]. Thrombin has also been shown to be an effective barrier disruptor that causes alteration in the mechanical environment of the endothelium with reports of increased cell-substrate tractions and average normal cell-cell stresses [7], [8], [46], [47]. It is currently un know how thapsigargin affects the mechanical environment of endothelial cells as well as how pharmacological disruptors interact with the maximum intercellular shear stress. To measure these changes in the mechanical environment of the endothelium the use of TFM and MSM are to be used. Disruption of the barrier function can be measured through a method called XPerT. XPerT uses the biotin-avidin complex two molecules that bind specifically and avidly to one another to visualize gaps in the endothelium[48]–[50]. This is done by using biotinylated collagen that can grow endothelial cells on top of and creating a monolayer, that if undisrupted, limits the ability for avidin to reach and bind to the biotinylated collagen. When avidin is fluorescently labeled and added to the media solution, the molecules that can travel through the gaps in the monolayer can attach to the biotinylated collagen. Because of the avid bond between avidin and biotin, when the solution with fluorescent avidin is rinsed away, the avidin attached to the biotin can be visualized and measured via fluorescent microscopy [48].

Endothelial Mechanics and Wound-Healing

The proliferation and migration of endothelial cells is a major aspect of wound-healing, a bottleneck, which is a prominent feature of the third stage in wound-healing known as the proliferation phase. During the cell proliferation phase of wound-healing, endothelial cells proliferate and migrate to the damaged wound area[15], [16], [51], [52]. This collective migration

is directed by leader cells that create a stress gradient that endothelial cells collectively follow through cell-cell junctions[3], [53]–[55]. Eventually, these cells are responsible for the formation of new blood vessels via angiogenesis. This is where endothelial cells proliferate and migrate into the area and create tubules that develop into new blood vessels. These new blood vessels provide oxygenation to the wounded area allowing other cells to migrate and reform the tissue. Speeding up this process is important as it is a bottleneck for wound-healing as insufficient or nonexistent angiogenesis can lead to chronic nonhealing wounds [15], [16], [56], [57]. The faster the cells can reach a damaged area, the sooner it can become revascularized and provide oxygen for other cells to migrate in for the wound-healing process to continue[3], [16], [52].

Electrical stimulation has been shown to stimulate endothelial cells into a pre-angiogenic response and direct endothelial movement. Magnetic stimulation has had mixed results in wound closure rates with many promising trials in improving wound healing in diabetic abscesses[58]. Electrical stimulation is believed to interact with endothelial cells through voltage differences as well as provide potential anti-inflammatory effects[59], [60]. to this To determine the effects of both types of therapies on endothelial cells, a preliminary set of scratch wound tests were performed for each therapy type[58].

Angiogenic Inhibition

As mentioned, wound-healing endothelial cells are the primary cells responsible for angiogenesis. Angiogenesis is responsible for creating blood vessels that provide oxygen and nutrients to an area that has demand outside of wound-healing as well and is an important function as humans' metabolic demands changes throughout their lives [61], [62]. However, angiogenesis plays an important role in the progression of a specific disease, cancer. Solid cancerous masses need

oxygenation from vasculature to grow. As a cancer mass grows the center of it becomes hypoxic and the cells start to send vascular growth factors to promote angiogenesis. This starts the creation of new blood vessels to support the cancerous tissue [61], [63]. This process can be restricted with the use of treatments that inhibit angiogenesis. This treatment can take the form of monoclonal antibodies that target growth factors such as vascular endothelial growth factor A (VEGF-A). Pharmaceuticals can also target growth factor receptors[64]–[66]. The issue with these pharmaceuticals is that prolonged exposure can lead to cardiovascular toxicity increasing the risk of heart dysfunctions, thrombosis, and bleeding [66], [67]. Despite the risks, the effectiveness of these treatments in limiting the size and growth rate makes them a valuable tool in cancer treatment though it is unable to cure cancer on their own. Because it is not a cure, it is usually coupled with a secondary treatment to eliminate cancer such as chemotherapy[64], [68]–[71].

Endothelial Mechanics and Diseases

The link between endothelial mechanics and specific diseases is currently unknown, but it is known that particular diseases damage the cell-cell and cell-substrate interactions that are key to the mechanical functions of the cell. Such diseases include diabetes, Covid, and heart disease. Diabetes is one disease that is known to degrade the endothelium and impact its function in both acting as a barrier and impacting wound-healing. This is believed to be caused by the glycation of proteins and lipids and of the cells. Glycation is the bonding of sugar to a secondary molecule. Glycation can interfere with the cell in direct and indirect ways. Glycation can happen directly to the cell-inhibiting proteins including junctional ones that are required for the cell to perform it's required function and indirectly by damaging and interfering with the functions of supporting cells and substrate, as well as interfering with signaling molecules such as nitric oxide that the

cells produce. This can inhibit wound-healing, increase vascular permeability leading to edema, and lead to other cardiovascular diseases including arterial stenosis and arteriosclerosis. Coronavirus is another disease that can directly damage surface proteins via the spike proteins that it uses to attach to the cell. These spike proteins can bind to and disable angiotensin converting enzyme 2 (ACE2) receptors causing the down regulation of a number of cell-cell junction including cx-43 leading to endothelial disfunction [11], [72]. The viral spike proteins have also shown to affect barrier function though RhoA activation[41]. Like diabetes this can lead to an increase in endothelial permeability possibly leading to degradation of the blood-brain barrier and pulmonary edema[11], [41].

In addition to barrier functions and being a major part of wound-healing endothelial cells help regulate vascular tone and aids in regulating blood pressure by being able to sense fluid shear on its surface. The cell is then able to through interactions with the smooth muscle cells using signaling molecules cause vasodilation or vasoconstriction. Heart disease has several detrimental effects on the mechanical functions of endothelial cells. Arteriosclerosis and arterial stenosis both alter and increase the stiffness of the substrate that endothelial cells grow on. In addition to this, the narrowing of the blood vessels and the reduced compliance of the vessel walls makes it more difficult for the endothelial cells to regulate blood pressure [73]–[75]

Traction Force Microscopy and Monolayer Stress Microscopy

Cells are, as part of their functions, are able to exert forces on the substrate and other cells they are attached to. This is done actively and passively through the cytoskeleton and cell-substrate

and cell-cell junctions. Traction Force microscopy uses the principles of proportional stress and strain to measure the forces cells exert on the surface of the substrate they are attached to also known as tractions. The substrate needs to be a soft substrate with a known stiffness where deformation can be measured for the force to be able to be calculated [76]–[79]. This has been accomplished in this experimental setup with fluorescent beads embedded in a 1.2KPa stiffness hydrogel. Comparing the substrate with deformations caused by cell traction and the substrate in stress-free state without cells allows for the calculation and mapping of the tractions with Fourier transform traction cytometry (FTTC) using the formula found in formula (1) [44], [80].

To determine the average normal and maximum shear stresses being transferred between cell-cell junctions, Monolayer Stress Microscopy (MSM) can be used under the boundary conditions that no forces are being exerted past the cell monolayer, that the monolayer is homogeneous, and has a uniform height. Newton's third law can be used to determine the amount of force being exerted between cells from the formula found in Figure 2[80].

CHAPTER THREE: RESEARCH METHODOLOGY ENDOTHELIAL PERMEABILITY

Traction Force Microscopy (TFM)

TFM is a common method to calculate the forces exerted by cells on their surrounding substrate also known as tractions. This is done by using a microscope to observe deformations in the substrate. TFM can be performed with a single-cell or multicell collections. Calculations of tractions can be performed in 2d if cells are grown in a fashion that has them spread across a single contiguous planer area also known as a monolayer. This monolayer can be constrained using micropatterns. These micropatterns were used to aid in the calculation of intercellular stresses by allowing the use of zero traction boundary conditions with the least amount of error. In addition, these unstressed regions were used to help eliminate errors due to subtle shifts in the microscope's stage during imaging via measuring and correcting pixel shift within MATLAB. With the substrate deformations gathered from imaging the fluorescent beads in the substrate a displacement field could be calculated and recorded using particle image velocimetry (PIV). With this displacement field, the tractions can be calculated using the Fourier Transform Traction Cytometry (FTTC) evaluated at z=0 developed by Butler et. al. [79] using the formulas below.

$$\vec{T} = FT_2^{-1}(\widetilde{\boldsymbol{K}^{-1}}\,\tilde{\vec{u}}) \qquad (1)$$

$$\boldsymbol{K}(r) = \frac{A}{r^3}\begin{bmatrix}(1-\sigma)r^2 + \sigma x^2 & \sigma\mathrm{xy} \\ \sigma\mathrm{xy} & (1-\sigma)\mathrm{r}^2 + \sigma\mathrm{y\hat{}2}\end{bmatrix} \qquad (2)$$

The formulas FTTC Tractions from the equation $\vec{u} = \vec{K} * \vec{T}$ evaluated at z = 0. u is the displacement field. K is Green's function mapping traction to displacement K ($|r - r'|$). T is traction.FT_2^{-1} is the inverse Fourier transform. Is A=(1+σ)/$\boldsymbol{\pi}$E, in which σ is Poisson's ratio E is Young's modulus [80]

Monolayer Stress Microscopy (MSM)

MSM is a method used to calculate intercellular stresses. Monolayer stress microscopy uses three required assumptions in the material nature of a cellular monolayer to calculate average normal and maximum shear stresses from the traction values from TFM. The first is that the cells within the monolayer act collectively as a homogeneous elastic material of uniform thickness. The second is that traction and the resulting intercellular forces in the z-direction are negligible. The third is that there are no tractions exerted past the monolayer's boundaries. With these assumptions, the boundary conditions can be set so that there are no intercellular stresses where the monolayer is not present. Tractions calculated from TFM can be placed into the Beltrami-Michell compatibility equation to determine the intercellular stresses. The Beltrami-Michell compatibility equation is derived from three different equations. The first is Newton's third law summarized into two dimensions due to the assumption of negligible forces in the z-direction. The assumptions of the cells acting as a homogenous elastic material allows the use of Saint-Venant's compatibility relations that links strain to displacement. The final equation used is Hooke's Law simplified to two dimensions due to a negligible z-component, which links strain to force. From this, the intercellular stresses can be calculated. From these calculated intercellular stresses, the minimum and maximum principal stresses can be calculated by rotating the stress tensor by the principal angle of 45 degrees to determine the maximum and minimum normal

stresses where the shear stress is zero. From these values, the average normal stress and maximum shear stress can be calculated and mapped across the monolayer (Figure 2).

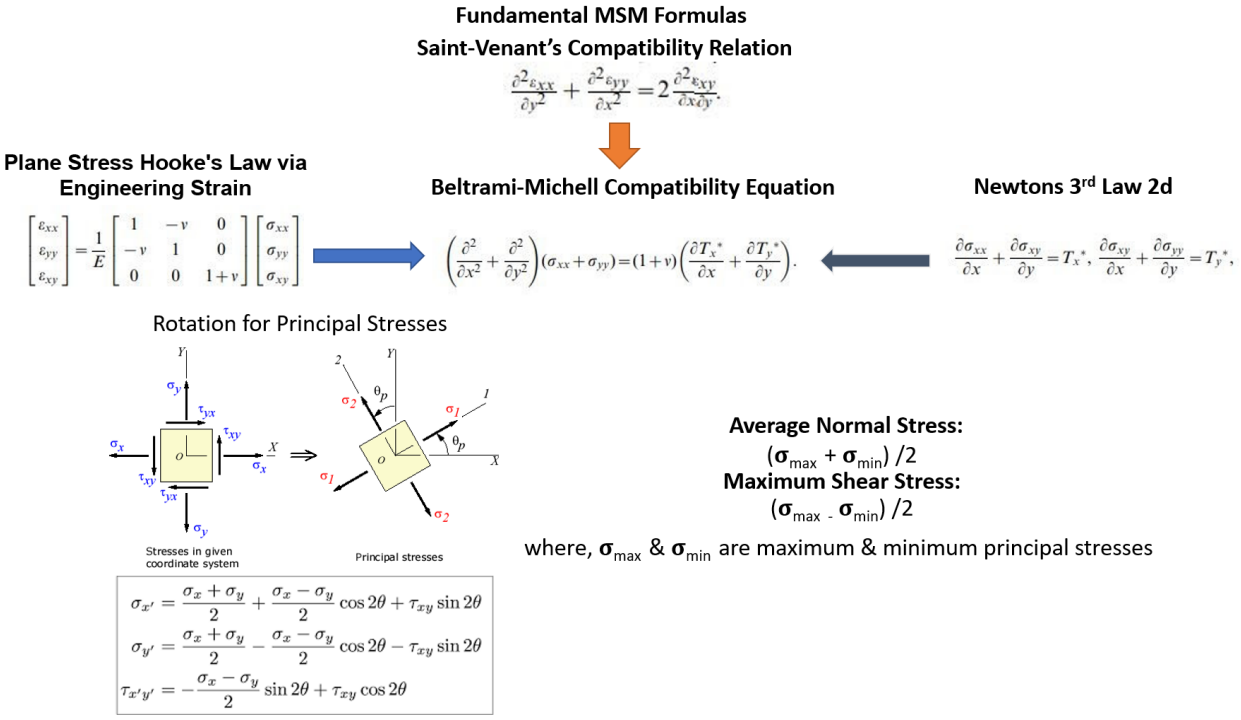

Figure 2: *Two-dimensional Beltrami-Michell compatibility equation used to determine intercellular stresses using the tractions from FTTC is derived from the combination of Hooke's Law, Saint-Venant's compatibility relation, and Newton's third law*[80].

In summary, with the use of fluorescent microscopy bead displacements were collected with the use of particle image velocimetry. These displacements were used to calculate cell-substrate tractions with TFM. These tractions are then able to be used to calculate the Intercellular stresses within the monolayer using the principles of stress, strain, and equal and opposite reactions with MSM.

CHAPTER FOUR: INVESTIGATION OF ENDOTHELIAL FUNCTIONAL MECHANICS OF ENDOTHELIAL PERMEABILITY

Abstract

Endothelial cells line the inner surface of all blood vessels and a host of cardiovascular as well as metabolic diseases are known to affect barrier permeability. Disease-induced permeability changes adversely the endothelium barrier functions subsequently leading to leaky blood vessel syndrome and retinopathy. Cell mechanics is believed to play a major role in regulating paracellular permeability. Our goal is to better understand the cell mechanics associated with the breakdown of the endothelial layer. Knowing both cell mechanics and permeability is tied to cell-cell junctions our experiment aims to compare both paracellular permeability and cellular biomechanics in an experiment that simultaneously monitors both. In this experiment, XPerT was used to measure endothelial monolayer permeability and traction force microscopy (TFM) was used to calculate the strength of the tractions endothelial cells exert on their substrate, monolayer stress microscopy (MSM) was used to calculate intercellular stresses and particle image velocimetry (PIV) was used to determine average cell velocity. Using these techniques undisrupted endothelial monolayers were compared to pharmacologically disrupted monolayers. Pharmaceutical disruptors were selected to target different cell-cell junctions. The disrupters selected were histamine, thrombin, thapsigargin, and 2-5 dihydroxychalcone.

Our results showed an increase in cell-substrate tractions and paracellular permeability and a decrease in average cell velocity for all forms of pharmacological disruption. The disruption of VE-cadherin with histamine and thapsigargin and Claudin-5 with thrombin saw a decrease in

average normal intercellular stresses, with no significant change with the disruption of Cx43 with Chalcone. Disruption with thrombin and histamine saw a decrease in average maximum shear intercellular stress. And disruption with chalcone and thapsigargin saw an increase in maximum shear intercellular stress.

Introduction

The endothelium acts as a semipermeable membrane that limits the amount of material into and out of the bloodstream. This barrier function is believed to be facilitated through the amount and organization of cell-cell junctions [4], [31], [44], [81]. Three types of junctions are expressed by endothelial cells, gap junctions, tight junctions, and adherens junctions [4]. All of these junctions have been shown to play a role in barrier function and cause an increase in endothelial permeability when disrupted [8], [10], [41], [43], [44], [48], [81]–[83]. For this study, these junction types are targeted with the use of pharmacological treatments that have been proven able to disrupt them. Adherens and tight junctions are the two most commonly associated with endothelial barrier functions by regulating paracellular permeability [32], [84]. Another cell-cell junction that is important to endothelial cells is gap junctions. Gap junctions are cell-cell junctions that allow small molecules and ionic signals to be transferred between cells [35], [36]. Prior studies by us have demonstrated that gap junctions also can carry intercellular stresses between cells. We previously demonstrated gap junction disruption to influence intercellular stresses using 2,5-dihydroxychalcone a molecule known to down-regulate connexin 43 expression[43]. Another molecule known to disrupt barrier function is thrombin. Thrombin is an enzyme that is well understood to be expressed during the process of blood clotting as it is required to convert fibrinogen to fibrin [47]. Thrombin also affects tight junctions by rapidly disassembling claudin-5

and has a slower effect on down-regulating VE-cadherin junctions [6], [85]–[87]. VE-cadherin Is an adherens junction protein unique to endothelial cells. This junctional protein plays a key role in regulating endothelial permeability, allows for leukocyte transmigration via bond reorganization, and potentially assists with leukocyte extravasation via tyrosine phosphorylation, endothelial proliferation, and angiogenesis [1], [12], [37], [38], [40] Pharmacological disruption of VE-cadherin via bond reorganization or junction disassembly has been shown to cause increased endothelial permeability. In this study, we also disrupt endothelial permeability by targeting VE-cadherin using the molecule thapsigargin. Thapsigargin depletes the endoplasmic reticulum (ER) of calcium by disabling its calcium pumps. The calcium from the ER ends accumulates in the cytoplasm inducing activation of Protein kinase C alpha leading to the disassembly of VE-cadherin [7]. An alternative method of disrupting adherens junctions is histamine. Histamine activates RhoA and causes phosphorylation of myosin, putting tension on the VE-cadherin junctions and opening gaps between the cells.

To measure how each type of pharmaceutical-induced disruption of the endothelium influences the cell mechanics of endothelial cells a variety of techniques were selected to gather data on cell-substrate tractions, intercellular stresses, monolayer permeability, and average cell velocities. Traction force microscopy is used to determine the magnitude and direction of the tractions the cells exert on the extracellular matrix (ECM) [30], [43], [77]–[79], [88], [89] Tractions are calculated using a substrate with a known stiffness and fluorescent beads. As the cells exert tractions on the substrate the beads are displaced by them. By measuring the distance and direction of displacement of the beads the tractions can be determined [30]. The substrate used is a 1.2kPa hydrogel with .5μm diameter embedded fluorescent microbeads. In addition, the data

from measuring the displacement of the embedded beads can be used to calculate the cell-substrate tractions with TFM. The cell-substrate tractions can then be used to calculate the forces exerted between cells through MSM [30], [43], [55], [80] Monolayer stress microscopy (MSM) utilizes the tractions and uses the finite element method (FEM) and Newton's force balance equation to determine the force exerted between the cells in a monolayer. These forces are converted to intercellular stresses based on the monolayer geometry.

Just as barrier disruption induces changes in the cell-derived mechanical forces mentioned above, this process also induces changes to endothelial permeability. The trans-endothelial electrical resistance (TEER) method is one of the most commonly used methods to characterize barrier permeability. TEER measures the resistance between two nodes across a membrane. As a membrane's barrier function breaks down the resistance between the two nodes drops [90]–[92]. However, the disadvantage of this technique is the inability to map and visualize locations of intracellular gaps and locations where the membrane is disrupted. This quality is important for this experiment as such a feature allows us to visually select locations to analyze that have been disrupted. The XPerT assay offers an alternative method to measure paracellular permeability and also provides visualization of paracellular gaps for a region of interest selection. This method uses fluorescently labeled avidin and biotinylated collagen to visualize the permeability of avidin protein and allows the visualization of paracellular gaps in a cellular monolayer[48]. A gap within the monolayer allows the fluorescently labeled avidin to penetrate the endothelial monolayer and attach to the biotinylated collagen coated on the substrate’s top surface. The avidin-biotin complex remains very stable since biotin and avidin have strong and specific binding properties [49], [93]. In this study, we target and disrupt specific junctions known to contribute to the

endothelial barrier function and monitor the changes in cell mechanics through cell-substrate tractions, cell-cell stresses, and cell velocity.

Materials And Methods

Cell Culture

The study was conducted using commercially purchased human umbilical vein endothelial cells (HUVECs). The HUVECs cells were cultured in medium 200 with large vessel endothelial cell supplement (LVES), all purchased from Thermo Fisher. The cells were grown in T25-75 flasks from Thermo Fisher Scientific coated in .1% gelatin from Sigma Life Science. Cells were incubated in an environment of 37°C and 5% CO_2.

Polyacrylamide Gel Fabrication

Protocol for the fabrication of polyacrylamide gel was adapted from the procedure used in. Steward et al. [30]. To act as a microscopic imaging compatible platform 35mm Cellvis glass bottom Petri dishes were selected. To allow for hydrogel attachment the glass bottom interior was treated with a bind silane solution for an hour. After the silane treatment the dishes were rinsed in DI water and dried air dried. The polyacrylamide gel stiffness was fabricated to mimic a healthy endothelium at 1.2Kpa. This was done by using a specifically ratioed mix of ultra-pure water, 40% acrylamide (Bio-Rad), and 2% bis-acrylamide (Bio-Rad). To visualize the tractions 0.5µm yellow-green, fluorescent Carboxylate-Modified Microspheres (Invitrogen) was added to this mix. To help improve the optical properties of the gel the mix was degassed in a vacuum chamber for an hour. To catalyze the polymerization of the polyacrylamide gel a 10% ammonia persulfate and then TEMED (N,N,N’,N’- tetramethylethane1,2-diamine) were added to the gel solution. To assure consistent gel thickness of approximately 100 µm, 24 µl of the gel solution

was added to each dish and then flattened into 100 µm tall cylinders using 18 mm diameter, .17mm thick, hydrophobic circular coverslips (Fisher Scientific). Coverslips were left on until the gel was completely polymerized and removed to allow for micropattern fabrication on the gel surface.

Cellular Micropattern Template Fabrication

Micropatterns were fabricated from polydimethylsiloxane (PDMS) cutouts as in prior studies with the following modification [30]. PDMS was with a mix of 20:1 Silicone to curing agent (both Dow Corning). The mix was then poured into a 100 mm petri dish to an approximate depth of 1mm. To eliminate bubbles the mix was degassed in a vacuum for 10 minutes. After being degassed the petri dish was then placed on a hot plate and cured at 70° overnight. After curing the PDMS film was removed from the petri dish and laid flat on a pane of hardened glass to provide a hard surface to it to adhere to. A 1cm diameter punch was used to cut disks from the film. The disks then had holes cut in them using a 2mm biopsy punch from a 1 cm diameter disk. The PDMS templates were then placed on the gel and pressed lightly to remove air between the PDMS and hydrogel before proceeding to collagen coating.

Biotinylated Collagen Preparation and Coating

The biotinylated collagen was used as the extracellular matrix material to allow for the use of the XPerT method [48]. The coating process was modified to allow the use of micropatterns on hydrogel. For this, a .1mg/ml solution of type one bovine collagen was used (Advanced Biomatrix) was created. The collagen was then biotinylated at a molar fold of 60 avidin to 1 collagen and incubated at 4 °C for 2 hours.

SANPAH Burning & Collagen I Coating

After incubation of the collagen, the gel dishes burned for the coating using sulfosuccinimidyl-6-(4-azido-2-nitrophenylamino) hexanoate (Sulfo-SANPAH; Proteochem) (SANPAH) in .01M HEPES solution (both fisher) for 20 minutes[30]. After this, the hydrogel was rinsed with HEPES. After the rinse, the .1mg/ml Biotinylated collagen is placed on the micropatterns and incubated overnight at 4 degrees °C. After incubation, excess collagen was gently rinsed with phosphate buffered saline (PBS).

Cell Transfer and Micropattern Seeding

After collagen treatment, cells can be incubated. After cells are transferred with the use of trypsin, 75ul is placed on each micropattern at an average cell density of 1.2 million cells/ml. The PDMS patterns are removed after 1 hour of incubation to allow for initial cell attachment. 2 ml of media was added, and cells were incubated for at least twenty-four hours until full confluency.

Cell-Cell Junction Disruption Drug Treatments

After 24 hours of incubation, cells were treated with media with one of the below barrier disrupters at concentrations known to disrupt endothelial cells [43], [48]. The barrier disruptors used were thrombin at .25 U/ml, chalcone at 2 µg/ml (10µM), histamine at 1.11µg/ml (10µM), and thapsigargin at .650 µg/ml (1µM). For the disruption conditions, micropatterned cells were exposed to the disruptors for two minutes before avidin treatment to allow time for paracellular gap formation before XPerT treatment.

XPerT Avidin Treatment

For avidin treatment, the XPerT method was used with the following modifications [48]. The avidin was added for three minutes to the cell micropatterns at a concentration of 33um/ml to the media with the barrier disruptor. After treatment, the barrier disruptor was removed, and the cells were rinsed three times with PBS. After rinsing standard media was added and the cells were imaged.

Time Lapse Microscopy

Cells were taken to the microscope for imaging immediately after XPerT treatment. Imaging data was collected using a Zeiss epifluorescence microscope equipped with a Hamamatsu camera. Images were taken with a 5x objective. A time-lapse was taken of the samples every five minutes for six hours. Images consisted of brightfield, red fluorescence image, and green fluorescence image. These images are for cell morphology visualization, paracellular gap visualization, and substrate deformation visualization, respectively. After time-lapse imaging cells were detached from the substrate using 10x trypsin. After all cells were detached from the substrate, stress-free images of the fluorescent beads were taken in the same positions as the time-lapse.

Gel Displacement Calculation

The displacement of the beads in the top layer of the hydrogel was calculated using a custom MATLAB-based PIV code. Within this code, the image was segmented into several overlapping square windows to assure an adequate bead count for displacement calculations. Peak Cross-correlation between the windows stressed and unstressed image was used to calculate the displacements for each window. The code performed this for every window created within the image. The displacement that was calculated for each stress-unstressed window pair was

calculated in the number of pixels displaced in the x and y. These pixel displacement values were converted into μm displacement values using the cameras pixel to micron conversion ratio. These values were recorded in a matrix with positions assigned by the central coordinates of the windows. This was done for each time point within the time-lapse sequence of images [30].

Traction Force Microscopy (TFM) Calculations

Traction force Microscopy as previously described [30] was used to calculate the cellular tractions. These calculations were performed by taking the prior calculated gel displacements and mapping the forces required along with the orientation of the force using the above stated FTTC Tractions fomula. These tractions were then maped out in a matrix with positions assigned alined with the responcibal displacments.

Monolayer Stress Microcopy (MSM)

The traction maps were then used to calculate the intercellular stresses. This was performed with a custom Fortran code. The code used the formulas in Figure 2 as mentioned above in order to use Newtons third law to determine the intercellular stresses. These calculated stresses were calculated and recorded in a two-dimensional stress tensor. From this stress tensor the minimum (σ_{min}) and maximum (σ_{max}) principal stresses were calculated by rotating the stress tensor to its 45 degrees. The average normal stress (σ_{avg}) and maximum shear stress (τ_{max}) were calculated using the formulas below (equation 3,4.

$$\sigma_{avg} = \frac{\sigma_{max}+\sigma_{min}}{2} \quad (3)$$

$$\tau_{max} = \frac{\sigma_{max}-\sigma_{min}}{2} \quad (4)$$

XPerT Avidin Fluorescence Measurement

Avidin fluorescent images were gathered with fluorescent microscopy. Due to the limited fluorescent intercity an extended exposure time of 10 seconds at 100% intensity was used for all images. Due to uptake of free avidin by the hydrogel background subtraction was performed by using MATLAB to find minimum intensity value from a region of interest (ROI) on the gel. The minimum value from this ROI was then subtracted from the entire image. The average fluorescent intensity was then gathered from an 500x500 pixel (650X650 μm) ROI selected from the center of the micropattern.

Cell Velocity Calculations

Cell Velocity was calculated using a custom PIV MATLAB code. This PIV MATLAB code is similar to the one used for measuring the bead displacements for TFM. Instead of beads, the code compared the phase images taken during time-lapse microscopy. The code was used to measure the pixel shift of the cells. The code compared each of the phase contrast images to the phase taken five minutes prior. These shifts were used with a pixel-to-distance that converted displacement in pixels to distance in μm, and an image number-to-time conversion factor to translate frame number difference to the amount of time passed, to calculate the average velocity of the cells contained within the monolayer.

Correlation Calculations

Data Gathered from phase, TFM, MSM and the background subtracted XPerT permeability fluorescence were overlayed on top of one another using a custom code in MATLAB. The phase imaging was used to select a 500x500 pixel (650X650 μm) ROI from the center of the micropattern. The ROI region was then used to extract the corresponding tractions, intercellular

stresses, and permeability florescence values from each respective data set in a 2D matrix. The matrix values for tractions, average normal stress, and maximum shear stress were correlated to XPerT Avidin Intensity via linear correlation using MATLAB (Figure 12).

Cell Identification for Cell Area, Cell Orientation, and Cell Eccentricity Measurements

The aspects of cell morphology and orientation were measured using MATLAB image processing toolbox. Cell area, cell orientation, and cell eccentricity were all calculated micropatterns for both disrupted and control conditions. This was done at the start of imaging and at the 3- and 6-hour time marks for comparison. In order for the computer to be able to identify the cells for analysis of the morphology and orientation the phase images needed to be converted into a form with clear boundaries. To do this phase-contrast images of the cellular monolayers were converted into binary images using MATLAB 'binarize' command using a contrast sensitivity thresh hold of .7. Background noise was reduced by using the 'bwareaopen' command that removed any pixel clusters under 100 pixels. After this the command 'watershed' was used to segment single cells. From this newly created binarized image cell features can be calculated using MATLAB.

Calculation of cell features and orientation.

Using the binarized images cells features could be calculated. Cell area, orientation and eccentricity were calculated using the 'regionprops' command in MATLAB. The command 'histcounts' was used to create binned histograms were used to categorize values. These bins were used to help visualize the data plotting the values, so each bin shares the same color value. 'regionprops' outputs area as a pixel count numbers for each cell, this value multiplied by the pixel to micron conversion factor for the camera to get the area in µm. Eccentricity was measured by using the formula e = c/a. Were e is eccentricity c is the measurement from the center of the cell

to the foci and a is the length of its semi major axis. This makes the range of eccentricity values from the eccentricity of 0 for a perfect cercal to an eccentricity of 1 for a line segment. The orientation was calculated by the orientation of the major axis of the cell. Output for orientation was between 90 and -90 degrees. To be able to get the average cell orientation values from the 4th quadrant (0 to -90) were moved to the second quadrant (90 to 180) by adding 180° (Figure 13).

Statistical Analysis

Data was collected from five micro patterns for each test condition (n=5). Statistical significance was calculated using a two-population t test. Statistical significance was tested between control values and those found in each disrupted condition for background-subtracted avidin permeability fluorescent intensity, tractions, average normal stress, and maximum shear stress.

Results

It was found that all the barrier disruptors caused an increase in permeability in comparison to the control. This was confirmed with increased avidin uptake for all barrier disruptors used. All disruption conditions have elevated RMS tractions. The intercellular stresses demonstrated major differences from one another (Table 1). Histamine had the most dramatic change with a major decrease for both average normal stress ≈37% and maximum shear stress ≈29%. Thapsigargin showed a decrease of ≈24% for average normal stress and an increase of ≈7% for maximum shear stress. Chalcone only shows a slight increase in normal stresses ≈4% a minor increase of ≈4% for maximum shear stresses. Thrombin Shows a major decrease ≈37% in normal stress but a moderate decrease ≈15% in maximum shear stress. This data shows that each form of disruption has its mechanical environment (Figures 4-7). However, areas of high permeability showed no spatial correlation with any cellular forces, potentially showing that even when

disrupted endothelial cells are still able to effectively transfer forces across the monolayer (Table 2). The analysis of the cell features did show some significant results with minor changes in cell areas for disruption under the thrombin and chalcone conditions (Figure 8). Under thrombin the cell area decreased ≈11% when disrupted and chalcone showed an increase in average cell area of ≈14% (Table 3). Looking at the average cell velocities, a general decrease can be seen across all disruption conditions. Thrombin had the largest decrease at ≈47%. Chalcone and thapsigargin both saw a slowdown of about ≈41%. Histamine had the smallest change with a velocity slowdown of ≈27% (Table 4, Figure 9). The results for thrombin do not entirely match prior results reported by Hardin. An increase in tractions was seen but a decrease in the average normal stress was seen in our results as opposed to their study[44]. This difference may be to the data being collected an hour after an hour of exposure to the disruption agent at a higher exposure concentration. As opposed to our short 5-minute exposure to the disruption agent to allow for the use of XPerT. Similar results are seen with the histamine results from Hardin with matching results for increasing tractions but a similar divergence with the average normal stresses also possibly due to a divergence in exposure time [44]. For chalcone using the 2ug/ml we see similar results for tractions but a difference in higher normal and shear stresses rather than lower values seen in Islam [43]. This also Is possibly due to the difference in disruptor exposure time of 6 hours.

Table 1: Table of cell mechanics results for permeability study with statistical significance.

Table Of Permeability and Cell Mechanics Results With Significance

Measurement	Control	Thrombin	Histamine	Chalcone	Thapsigargin
Avidin Fluorescence (Counts)	1096±45	2303±54	3147±82	1814±21	1553±21
Percent Difference		110%	180%	66%	42%
Significance		Significant	Significant	Significant	Significant
RMS Tractions (Pa)	12.4±.2	26.6±.9	17.4±.2	26.4±1.2	28.9±.5
Percent Difference		115%	40%	113%	133%
Significance		Significant	Significant	Significant	Significant
Average Normal Stress (Pa)	229.2±5.8	143.5±6.5	143.5±5.7	237.3±3.5	173.4±5.3
Percent Difference		-37%	-37%	4%	-24%
Significance		Significant	Significant	Not Significant	Significant
Maximum Shear Stress (Pa)	137.8±2.2	117.8±4.3	97.4±1.6	154.6±5.5	147.8±3.8
Percent Difference		-15%	-29%	12%	7%
Significance		Significant	Significant	Significant	Significant

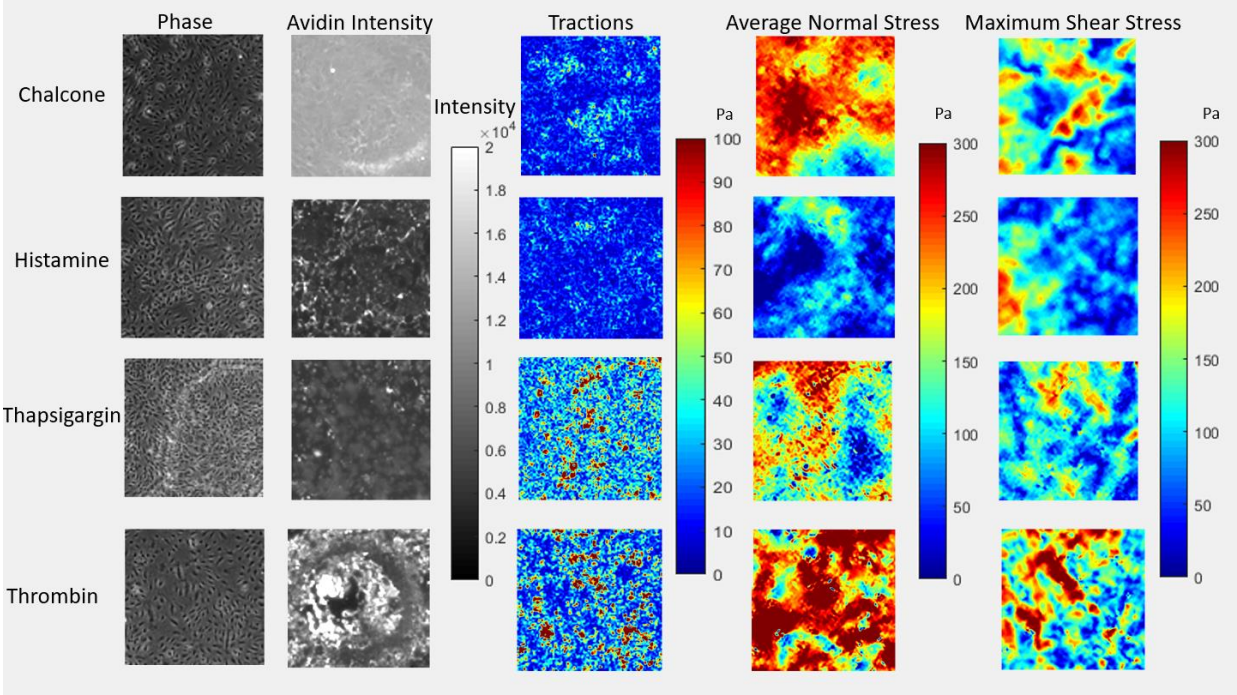

Figure 3:*Columns From left to right: Phase, avidin fluorescence, RMS tractions average normal stress and maximum shear stress for each disrupted condition.*

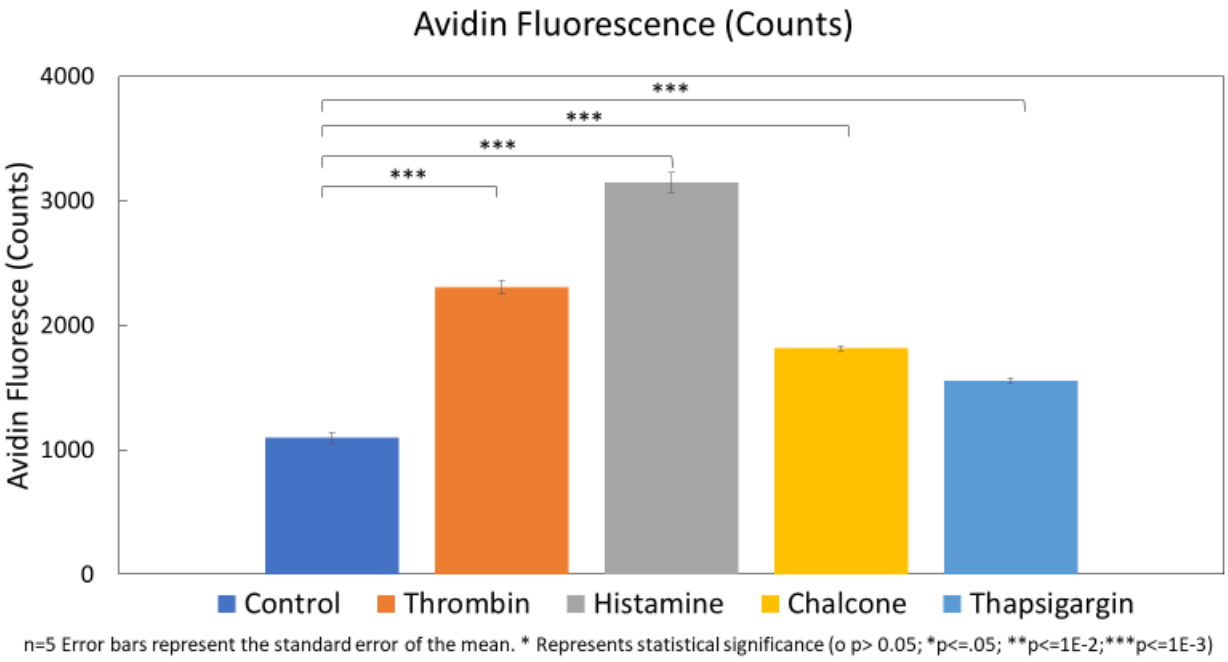

Figure 4: *Results for permeability measurements via avidin fluoresce post background subtraction.*

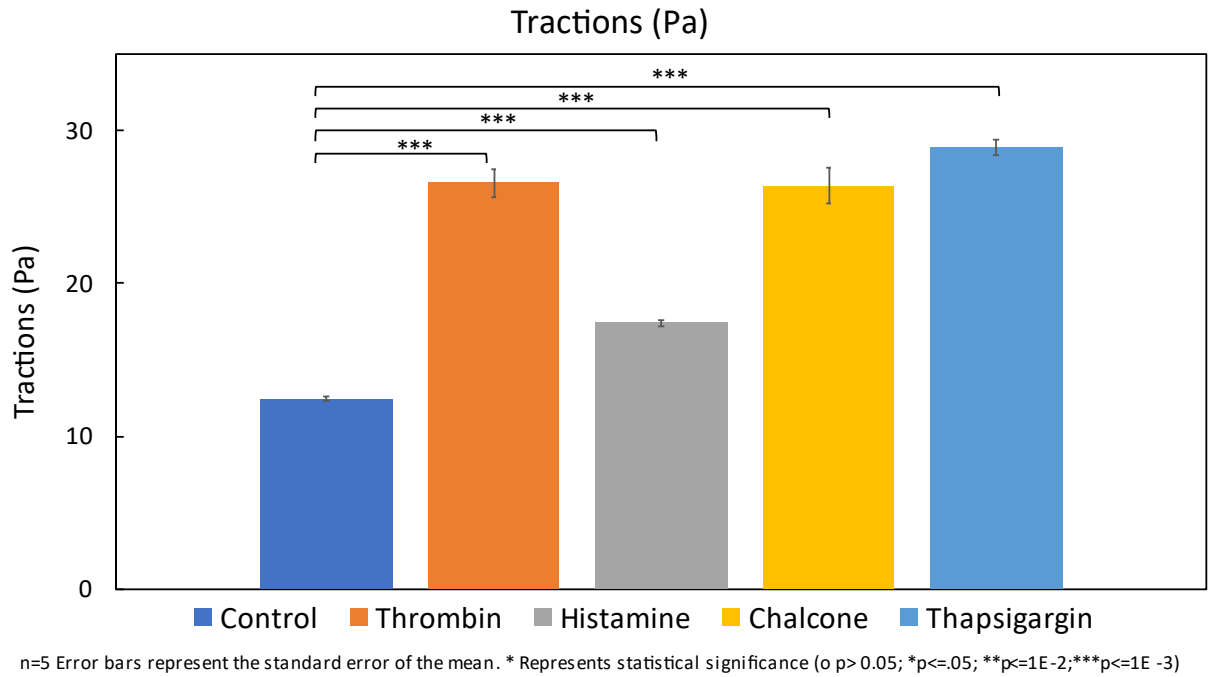

Figure 5: *Results for average cell substrate tractions*

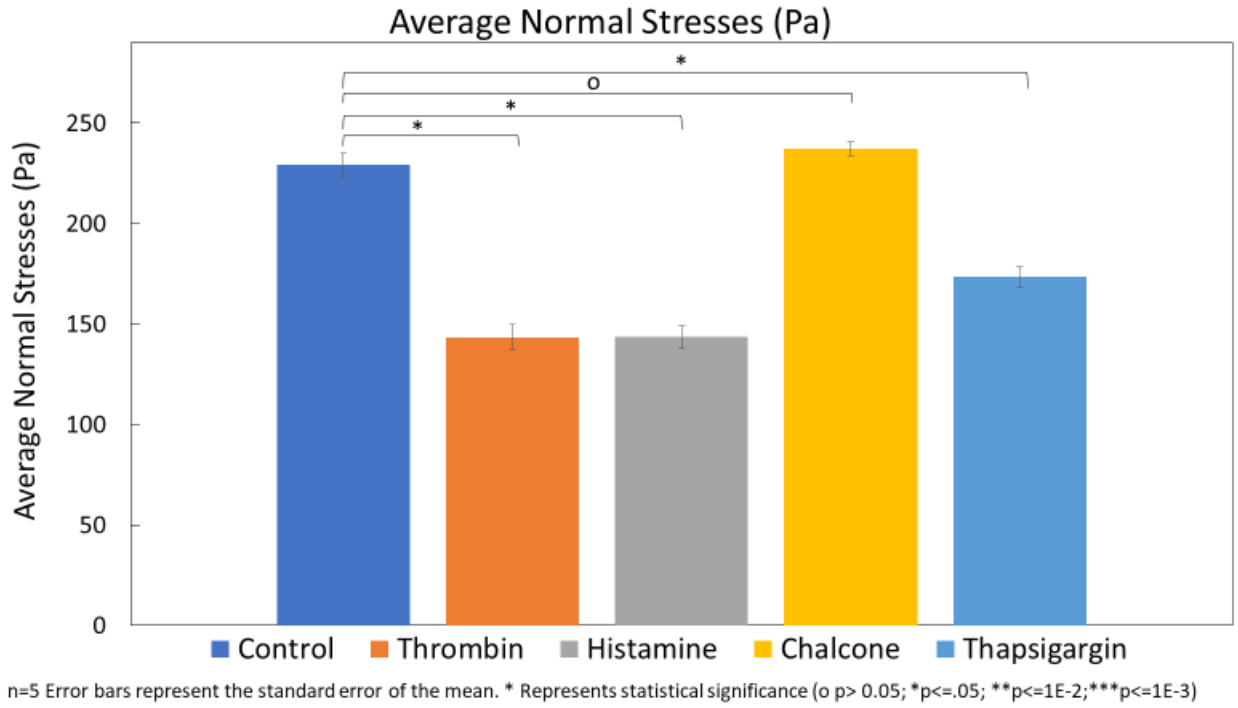

Figure 6: Results for average cell-cell normal stress

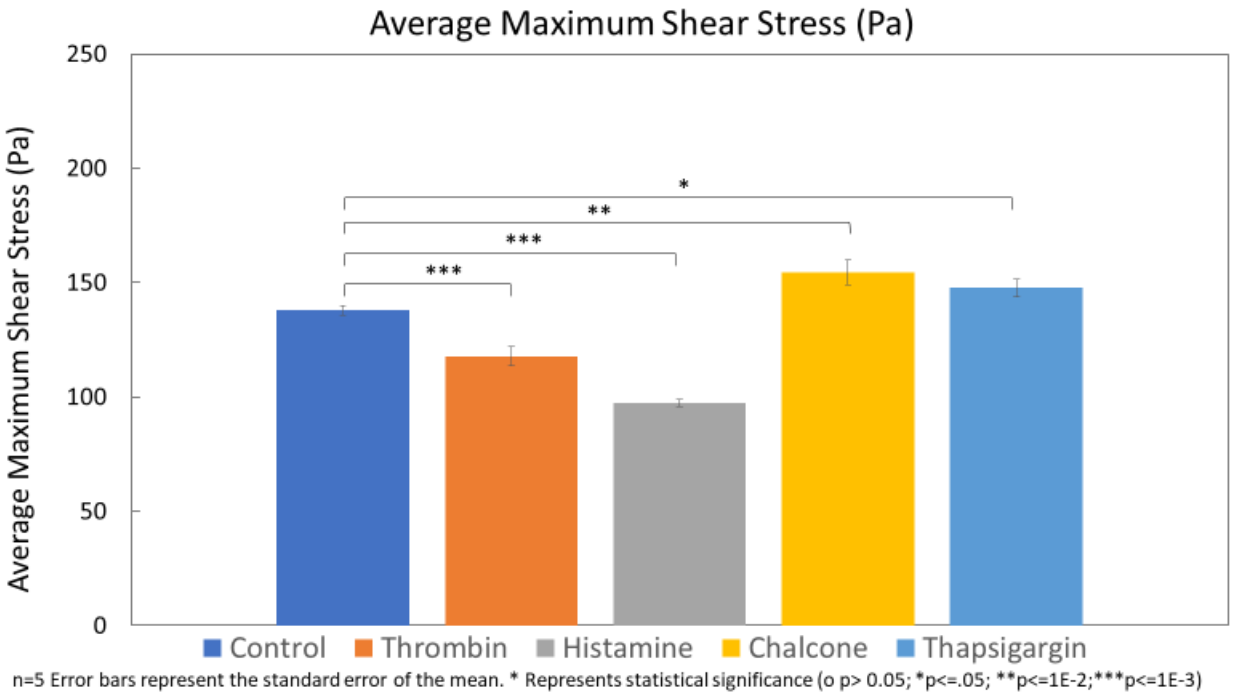

Figure 7: *Results for average cell-cell maximum shear stress.*

Table 2: *Local correlations between avidin fluorescence and Cell Mechanics minimum value of .2 being significant.*

Correlation Coefficients (r) Between Avidin Florescence and Cell Mechanics

Measurement	Control	Thrombin	Histamine	Chalcone	Thapsigargin
RMS Tractions (Pa)	0.0219	0.0196	0.00745	0.031221	0.0106
Average Normal Stress (Pa)	0.0651	0.0316	0.03165	0.07884	0.0261
Maximum Shear Stress (Pa)	0.0658	0.0392	0.01751	0.061565	0.01962

Table 3:*Table of Cell Features with Significance.*

Table Cell Features With Significance

Measurement	Control	Thrombin	Histamine	Chalcone	Thapsigargin
Average Cell Area (µm*µm)	341.544±2.469	304.236±2.35	358.394±2.642	388.371±9.068	319.903±14.960
Percent Difference		-11%	5%	14%	-6%
Significance		Significant	Not Sigificant	Significant	Not Significant
Average Eccentricity	.7991±.0015	.8471±.0017	.8223±.0020	.8261±.0022	0.8023±.0015
Percent Difference		6%	3%	3%	4%
Significance		Not Sigificant	Not Sigificant	Not Sigificant	Not Sigificant
Average Orientation (degees)	88.54°±.52	87.40°±.67	90.99°±.75	88.67°±.82	89.29°±.53
Significance		Not Sigificant	Not Sigificant	Not Sigificant	Not Sigificant

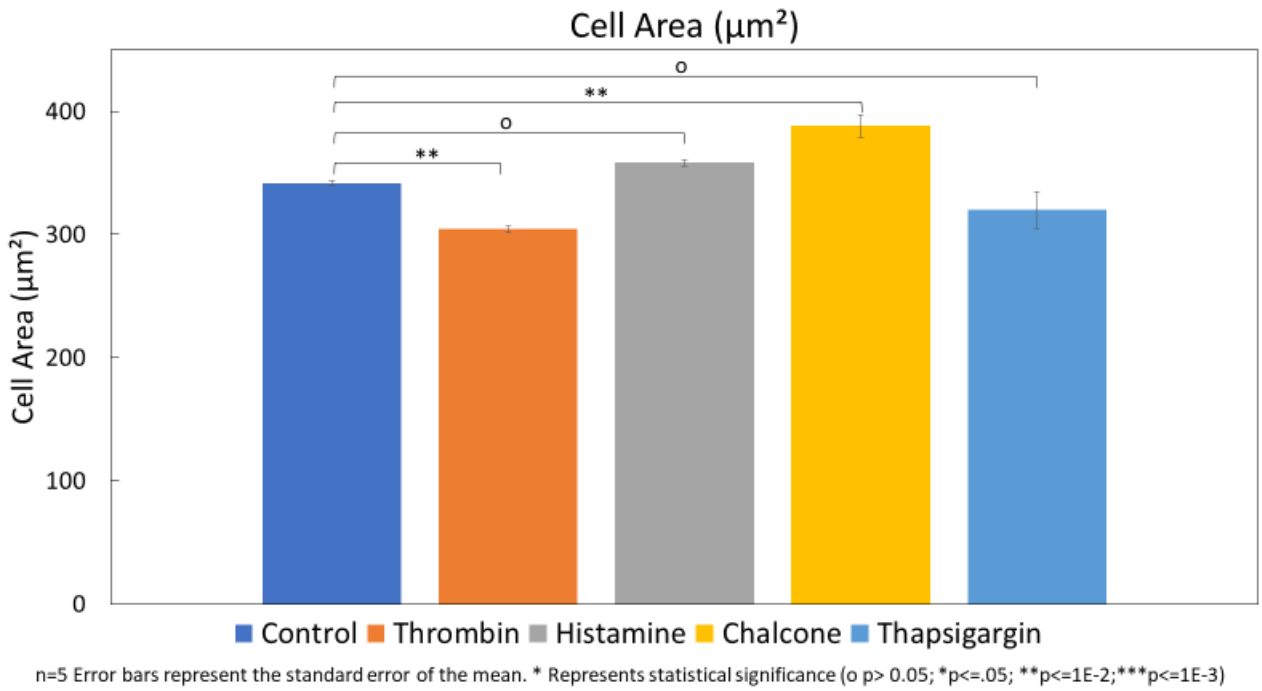

Figure 8: *Average cell area under disruption*

Table 4: *Average cell velocity under disruption conditions*

Measurement	Control	Thrombin	Histamine	Chalcone	Thapsigargin
Velocity µm/min	0.295±.004	0.156±.004	0.211±.004	0.175±.004	0.176±.005
Difference From Control		-47.30%	-28.60%	-40.80%	-41.00%
Significance		Significant	Significant	Significant	Significant

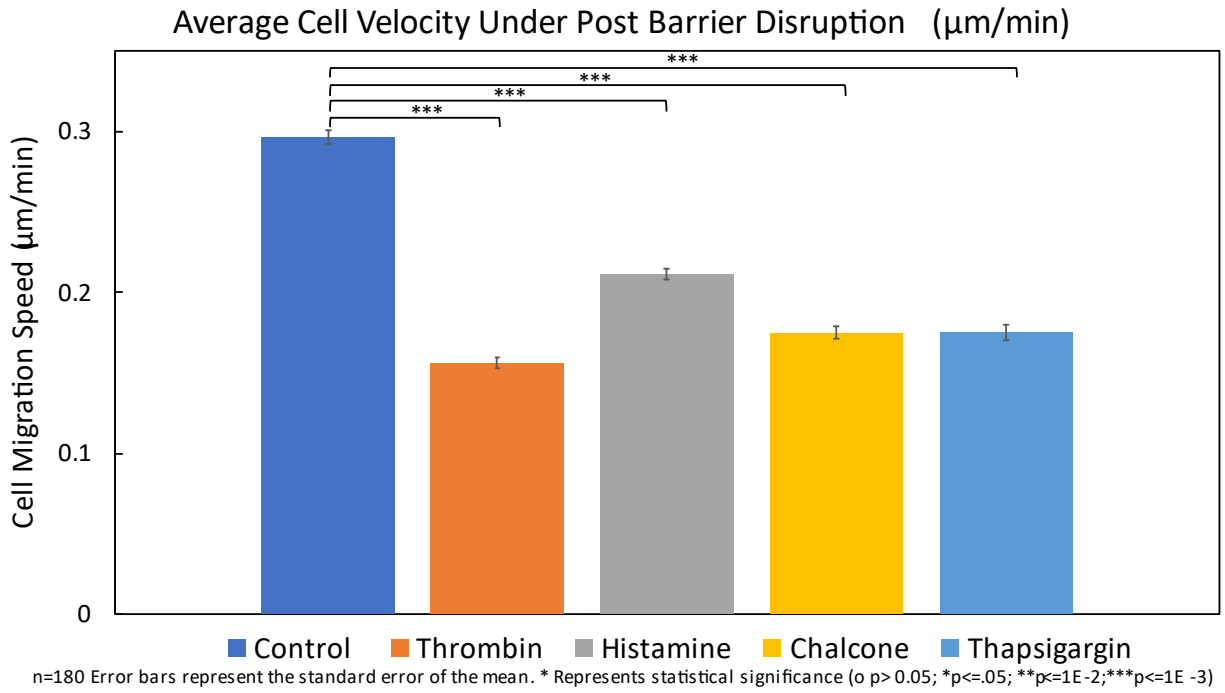

Figure 9: Average cell velocity under disruption conditions

Discussion And Conclusions

With these studies it has been shown that the XPerT method can be used in concert with traction force microscopy and monolayer stress microscopy opening the doors for new study types. The different mechanical profiles for each barrier disruptor show that each form of barrier disruption is not the same and that cells adapt and distribute forces differently to each type of disruptor.

There is one trend, across all the disrupters tested is that post disruption tractions exerted by the cells are increased. This is an important consideration going forward when looking at different forms of pathology that cause endothelial disruption as this represents increased strain on the cell substrate. We have also uncovered that there is not a local correlation between gaps formed by monolayer disruption and tractions, average normal and maximum shear stresses. This could be due to several factors including that despite being in a disrupted state cells still are able to distribute forces between one another delocalizing intercellular stresses. Is also seen that histamine disruption has the lowest negative effect of cell migration. This may be to the preservation of the cell-cell junctions during disruption allowing for better post exposure communication of cell mechanics.

Supplementary

XPerT was used to measure permeability using the avidin biotin complex. Avidin and biotin both bind to each other with a large amount of strength and specificity allowing them to be used as fluorescent markers. Biotin labeled collagen was used as the ECM for the endothelial cells. Fluorescent avidin was used as a marker for permeability. This is because avidin is small enough to travel through the paracellular gaps in endothelial cells and attach to the biotinylated collagen where it will remain and can be used to visualize the locations of these paracellular gaps and measure permeability.

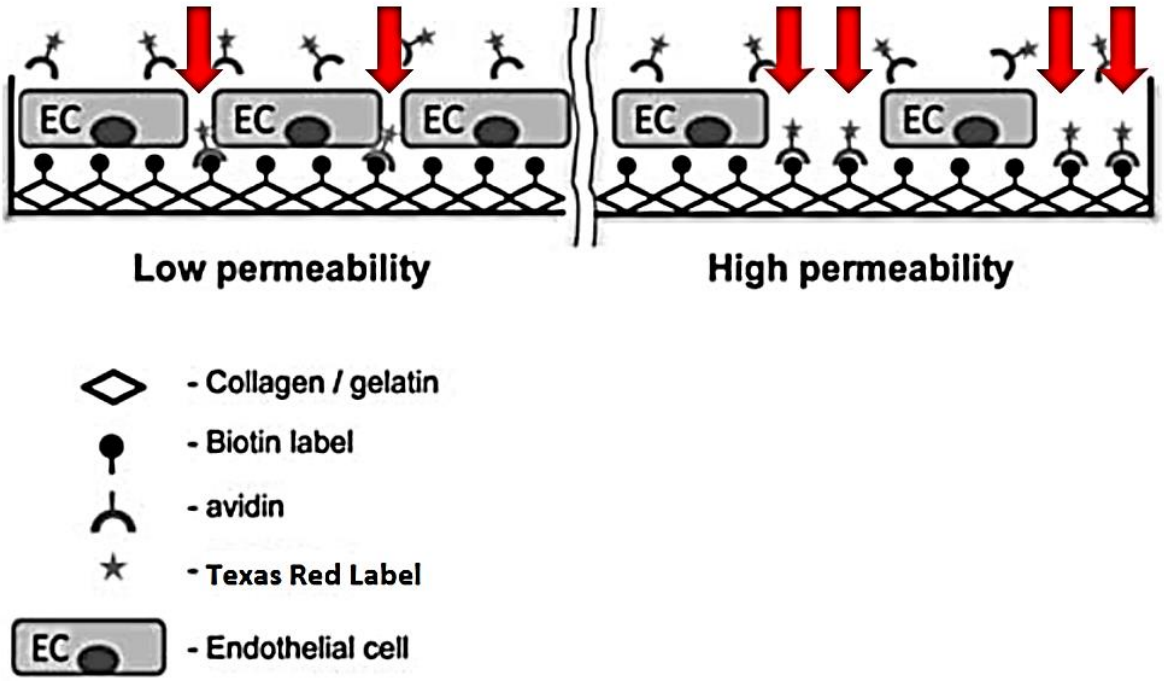

Figure 10: *XPerT Avidin method of measuring permeability. Red arrows point out paracellular gaps were fluorescently labeled avidin can pass between endothelial cells and attach to the Collagen substrate* [48].

Micropatterns were disrupted and monitored for 3 hours as far as avidin fluorescent using XPerT. This was done using live cells in order to be able to use TFM and MSM. The limitation of this is Phagocytosis of the avidin by the HUVECs cells causing fluorescence to concentrate within the cells after the 3-hour mark limiting the length of the study.

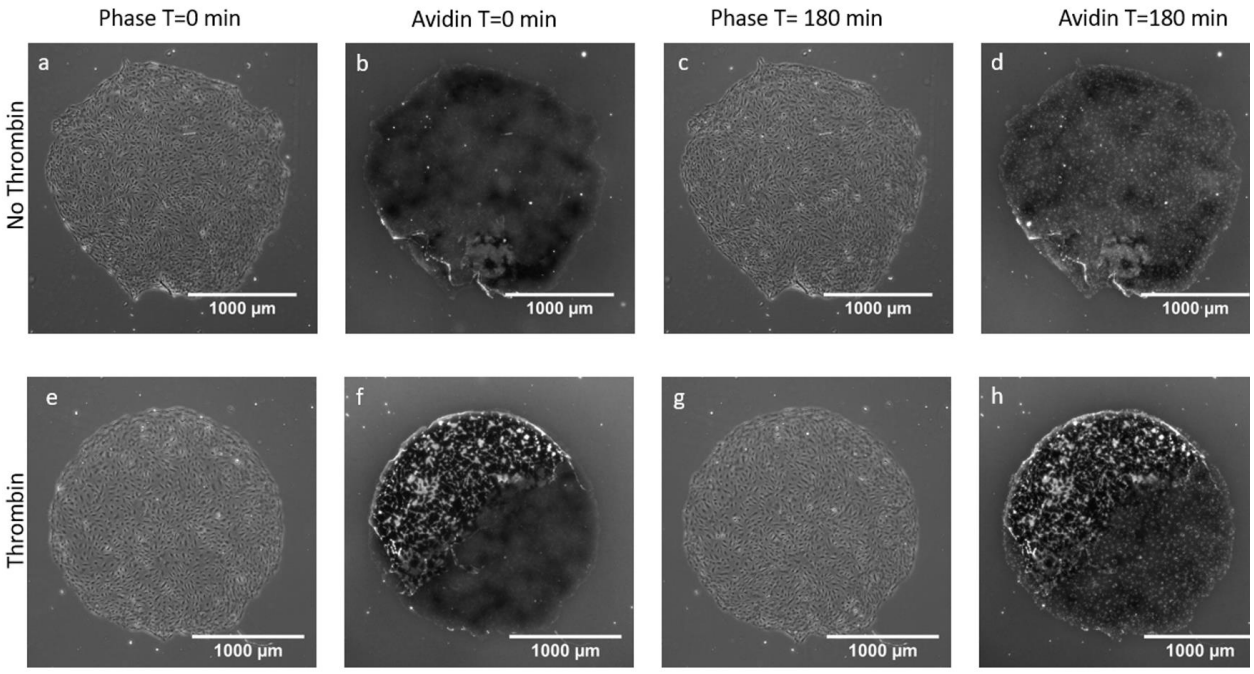

Figure 11: *Micro patterned HUVECSs cells and avidin permeability at imaging start and after 180 min for control and thrombin treatment conditions. a-d) show the low avidin penetration within the control group. f-h) shows avidin florescence uptake on the substrate in area disrupted by thrombin. d,h) Note: avidin uptake by cells at 180 min mark.*

Disruptors were selected for their ability to target a different set of cell-cell junctions. The method of disruptions is also worth noting as Histamine does influence VE-cadherin junctions along with other Adherens junctions but through the tension of actin filaments.

Table 5: *Set of disruptors used and targeted junctions *VE-cadherin at higher concentrations.*

Disruptor	Dosage	Target	Method	Source
Thrombin	.25 U/ml	Tight Junction: Claudin-5*	Down regulating claudin-5	[47]
Chalcone	2 µg/ml (10µM)	Gap Junction: Cx43	Cx43 Phosphorylation	[43]
Histamine	1.11µg/ml (10µM)	All Adherens Junctions	Cellular Tension	[8]
Thapsigargin	.650 µg/ml (1µM).	Adherens Junction: VE-cadherin	Activation of PKCα	[7]

MATLAB was used to calculate the correlations between avidin intensity and cell-substrate tractions, cell-cell maximum shear, and cell-cell average normal stresses. This was done using MATLAB's image cropping tools to select a square region of interest to extract matrix values for each form the same area.

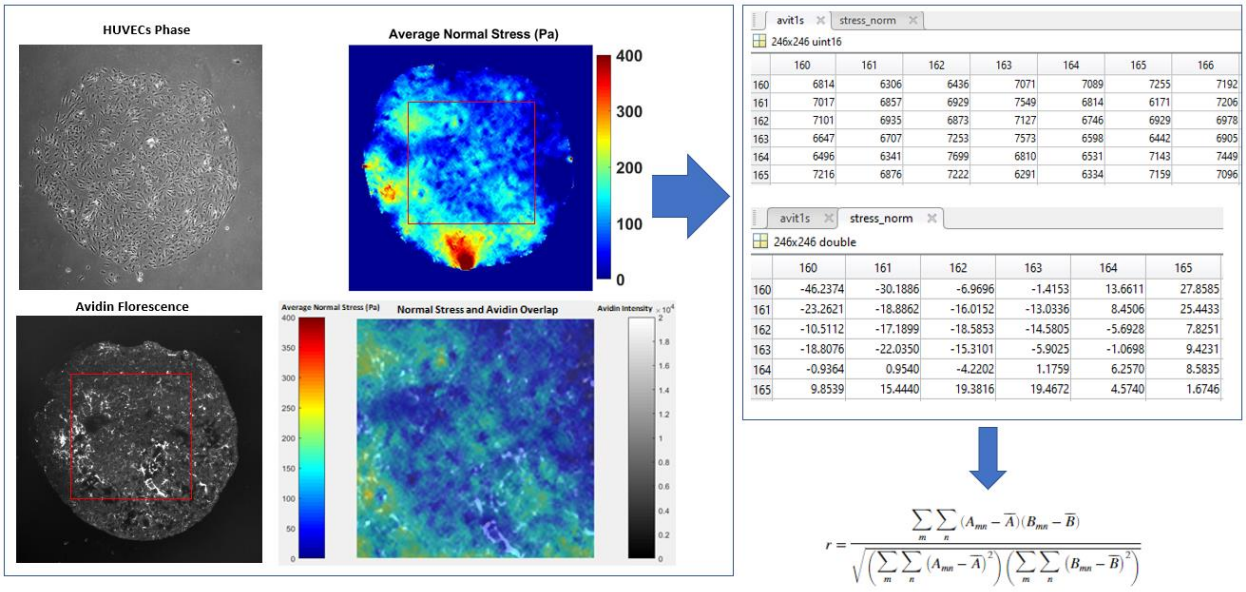

Figure 12: *Cropping of region of both avidin florescence and average normal stress overlayed on top of one another. Cropped data matrixes are then used to calculate the correlation coefficient between the two matrixes.*

For cell features to be quantified using MATLAB the phase image first had to be converted into a form that could be easily recognized with photo analysis. To do this the image was binarized into a pure black or white image. From this black and white image MATLAB was used to calculate the eccentricity cell area and orientation of each cell within the monolayer.

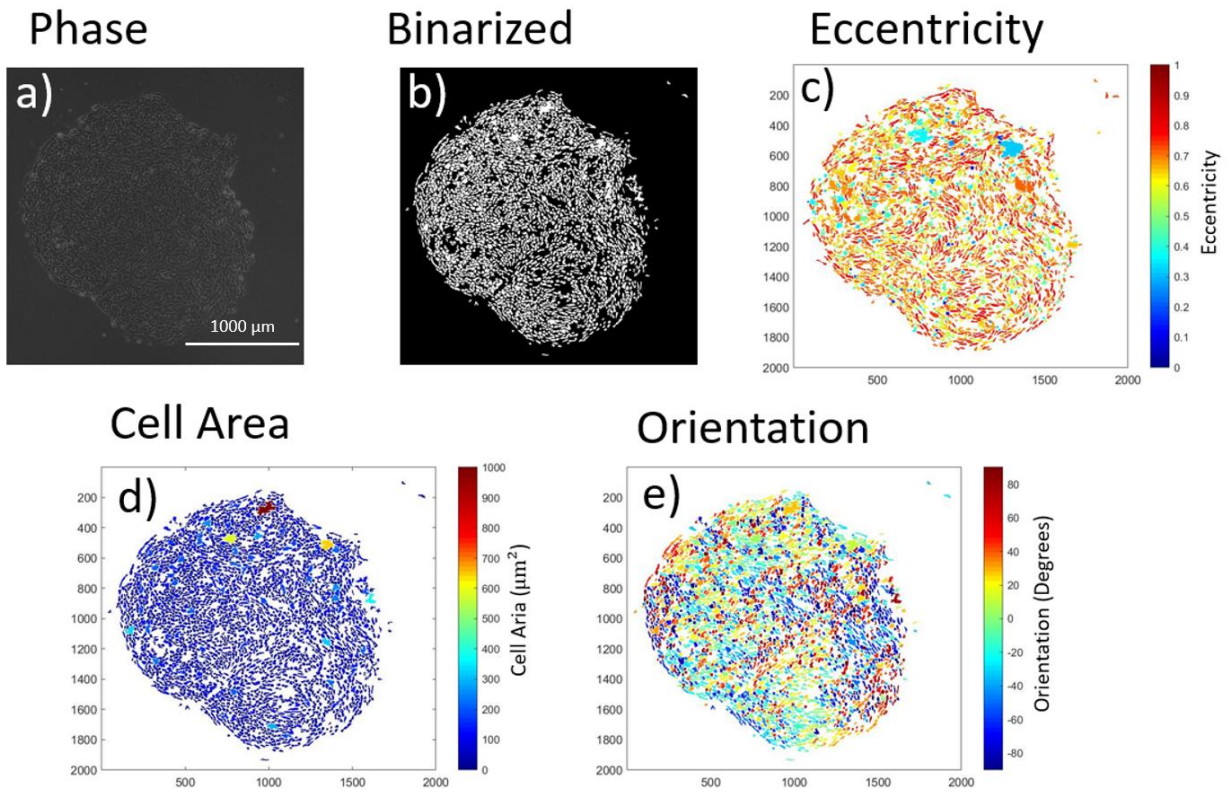

Figure 13: *Cell Feature extraction. a) phase image is collected. b) phase image is binerized into black and white image. c) Eccentricity values are callculated for each cell. d) cell areas are callculated fromcluster pixle counts. e) Orientation is calculated for each cell.*

CHAPTER FIVE: EFFECTS OF MAGNETIC AND ELECTRICAL FIELD EXPOSURE TO ENDOTHELIAL CELL WOUND-HEALING.

Abstract

The use of magnetic fields and electrical stimulation have been a subject of study to discover a way to increase the speed of wound-healing and has been studied in animal and cell models with mixed results. Both pulsed and static magnetic and electrical fields have been looked at with interest in developing therapies to help with wound recovery time. To get an improved model using human cells we used an invitro scratch assay wound-healing model to determine the effect of different strength magnetic fields on the endothelial cells wound closure rates and average migration speeds. For this model we used endothelial cells to get a better idea of how magnetic fields can influence this cell type during wound-healing due to the key role they play in the process.

Wound closure rates and average cell velocities for HUVECs were measured under a static magnetic field of 3700, 1152, 650 and 50G via scratch tests. The results found a reduction in wound-healing for HUVECs cells when exposed to a static magnetic field of 3700, 1152, and 650. This slower rate of wound closure was generally seen along with an accompanying slow down in average cell velocities. This hints that angiogenesis may slow down under these conditions. For the 50G magnetic field there was a large increase in both wound closure rates and average cell velocities for the attractive magnetic field conditions with a slowdown in closure rates and cell velocities in the repulsive orientation of the magnetic field. In addition to magnetic stimulation, a set of electrical stimulation experiments were conducted using a .75mv/mm potential pulsed voltage field. It was seen

that the electrical stimulation was effective at improving both average cell velocity and wound closure times when oriented parallel to the voltage potential.

Introduction

The proliferation and migration of endothelial cells are major aspects of wound-healing. Both processes are also a bottleneck for complete wound-healing and are prominent features of the third stage in wound-healing known as the cell proliferation phase [15], [16], [94]–[96]. It is believed this collective migration is directed by leader cells that create a stress gradient that endothelial cells collectively follow. This stress gradient is carried through cell-cell junctions[95], [96]. Eventually, the migrating endothelial cells are responsible for the formation of new blood vessels via angiogenesis. Angiogenesis is where endothelial cells proliferate and migrate into the ischemic area and differentiate to create tubules that develop into new blood vessels. These new blood vessels provide oxygenation to the wounded area allowing other cells to migrate and repair the tissue. Speeding up this process is important as insufficient or nonexistent angiogenesis can lead to chronic nonhealing wounds. The faster the cells can reach a damaged area the sooner the anoxic wound space can become revascularized and provide oxygen for other cells to migrate in for the wound-healing process to continue [15], [16], [52], [94].

Electrical stimulation has been shown to stimulate endothelial cells into a pre-angiogenic response becoming elongated to be more motile and facilitate endothelial movement in individual cells. This is believed to indicate that the cells are responsive to such stimulation on an individual level [14], [97], [98]. Yet magnetic stimulation has had mixed results in wound-healing rates with some studies have showing potential wound-healing

increases while others have shown negligible increases to overall wound-healing in mice, rat, and chicken models [58], [59]. The therapies are believed to interact with endothelial cells via voltage gradients that imitates the natural phenomena seen at injury sites as well as provide potential anti-inflammatory effects [58]–[60], [97]–[99]. To determine the effects of both magnetic and electrical therapies on endothelial cells are effective at improving wound healing, a set of scratch assays were performed to determine the effectiveness of magnetic therapy.

Materials and Methods

Cell Culture

For the magnetic wound-healing experiments, polystyrene tissue culture plates (manufactured by Techno Plastic Products) were coated with .1% collagen (Sigma Alrich). HUVECs were seeded in 11mm diameter 12 well polystyrene Tissue culture plates and grown to 100% confluency in media 200 with large vessel endothelial supplement (Fisher Scientific). Cells were rinsed with phosphate-buffered saline (Corning) and new media was added every 2 days until this confluency was met and the scratch test could be started. For the electrical stimulation setup 35mm glass bottom dishes (Cellvis) were used.

Wound-Healing Assay

The scratch test to determine wound-healing was done in the confluent 12-well dishes or 35mm glass bottom dishes. Scratches were performed with a 10 µl pipet tip (Fisherbrand). This produced a scratch width on average of 353 µm. Scratches were made in either a vertical or horizontal orientation depending on the experiment requirements (Figure 27). A straight scratch was performed with the pipet tip with the aid of a straight edge. Scratches were made through

the center of the well over the entire monolayer. The 12 well was then placed on an epifluorescence microscope for imaging.

Permanent Magnet Experimental Setup

For the experiments that used a magnetic field generated from permanent magnets, the magnets were placed at the top and distal and proximal edges of the 12-well tray. Two rectangular ferrite ceramic magnets were used for the ≈3700G condition, for the 1,152 G condition two neodymium magnets were used and, for the ≈625G two polymer ferrite magnets were used. These magnets were placed in attractive and repulsive magnetic polarity arrangements with six of the scratch test wells arranged between the two magnets for observation with time-lapse microscopy (Figure 24,25).

Tangent Galvanometer Experimental Setup

Two tangent field galvanometers were placed at the left and right hand of the twelve-well tray and tuned so that they produced a magnetic field of 50G at the center of the 12-well in an attractive configuration. For the repulsive condition, the current through the second galvanometer was reversed and the experiment was conducted again under the same voltage and current settings (Figure 26).

Electrical Stimulation Setup

Electrical stimulation was performed with an open-source waveform generator[100]. The stimulation cycle chosen was a 40% work cycle square wave form of 75 mv/mm a voltage that has been shown to have a positive effect increasing average cell migration speeds.[14], [97],

[98]Voltage was applied over the wound area with two parallel pure zinc wire nodes to prevent issues with corrosion (Figure 28,29).

Time Lapse Microscopy

Time-lapse microcopy was carried out in a similar fashion as the prior study with the marked changes [30]. Only phase images were collected at 10-minute intervals until complete wound closure was observed.

Wound-Healing Measurements

Wound-healing measurements were done manually using FIJI-ImageJ. Using the measurement tools, a 1mm long wound section width was measured throughout the wound-healing process until closure. The closure rate was calculated simply by measuring the original width and then dividing it by the time it took for the wound to close. This was done for 18 samples under each test condition mentioned above (Figure31).

Cell Velocity Calculations

Average cell velocity was calculated for the wound-healing process of each condition with particle image velocimetry in a custom MATLAB code. Average velocities were determined over the first six hours of wound-healing for each wound-healing condition. This duration of time was chosen as no wound samples closed in under six hours. This assured that all data would have the same number of samples for each condition and that all velocity data would be before wound closure. This was done over 18 samples every 10 minutes for 6 hours for each test condition.

Results

The major finding is that the lower-strength magnetic field of 50G seems to have a stronger effect on both wound closure and the average cell velocity of endothelial cells than the stronger magnetic field conditions. With the 3700G condition would closure times seeing, a non-significant decrease of 7% is seen for the repulsive vertical (RV) and attractive vertical (AV) conditions, and significant but minor decreases of 9% and 18% for attractive horizontal (AH) and repulsive horizontal (RH) conditions (Figure 14). At 3700G average cell velocities a significant but small increase of 3% is seen for the AH conditions. The other 3700G conditions had minor but significant cell velocity decreases of 8%,3%, and 3% for AV, RH, and RV conditions respectively with no significant change for AH (Figure 15, Table 6). For the 1152G permanent magnet field, none of the wound closure time results were significant with a decrease of 16%, 13%, 9%, and 14% for AH, AV, RH, and RV conditions respectively (Figure 16). For average cell velocity, AH had an insignificant decrease of 1%. The other conditions had a significant decrease of 19%, 13%, and 19% for AV, RH, and RV respectively (Figure 17, Table 4). For the lower strength magnetic field conditions, consistent significant changes start to appear for both wound closure rates and average cell velocity. For the ≈650G permanent magnet wound closure times, we see a moderate decrease in the wound closure rate of 35%, 24%, 45%, and 30% for AH, AV, RH, and RV conditions (Figure 18). Average cell velocity also shows decreases across the board of 20%, 22%, 21%, and 9% for AH, AV, RH, and RV (Figure 19, Table 8). The 50G field created by the tangent field galvanometer created the strongest influence on both wound closure rate and average cell velocity. For the attractive conditions, there was an increase in both wound closure rate and average cell velocity. For wound closure rate there was an increase of 120% and 140% for AH and

AV conditions along with an average cell velocity increase of 84% and 98%. For the repulsive condition at the same intensity, we see a large decrease in wound closure rates and average cell velocity. With a decrease in wound closure rates of 69% and 63% and a decrease in average cell velocity of 54% and 53%, respectively for RH and RV conditions. From these results, we can see that with the galvanometer produced 50G attractive field is the only one that resulted in faster wound closure results. For the 3700, 1152, and 650G conditions, the wound closure rate was reduced. For electrical stimulation it was observed that electrical stimulation under a voltage potential of 75 mv/mm perpendicular to the wound an increase in wound-healing of ≈23% can be seen while the parallel did not see a significant increase in wound closure times (Figure 22). Both wound orientations saw an increase in average cell velocity of ≈11% (Figure 23). This implies that the direction of the voltage potential is important to the effectiveness of the treatment (Table 10).

Table 6:*Table Of wound closure rates and average cell velocity results with significance at ≈3700 Gauss permanent magnet field*

Table Of Wound Closure Rates and Average Cell Velocity Results With Significance at ≈3700G

Measurement	Control	Attractive Horizontal	Attractive Vertical	Repulsive Horizontal	Repulsive Vertical
Average Closure Rate (µm/m)	.4408±.0137	0.4061±.0138	.4093±.0233	.3630±.0211	0.4094±.0079
Percent Difference		-9%	-7%	-18%	-7%
Significance		Significant	Not Significant	Significant	Not Significant
Average Cell Velocity (µm/m)	0.4694±0.0012	.4838±.0012	.4334±.0013	0.3457±.0008	.4094±.0079
Percent Difference		3%	-8%	-3%	-3%
Significance		Significant	Significant	Significant	Significant

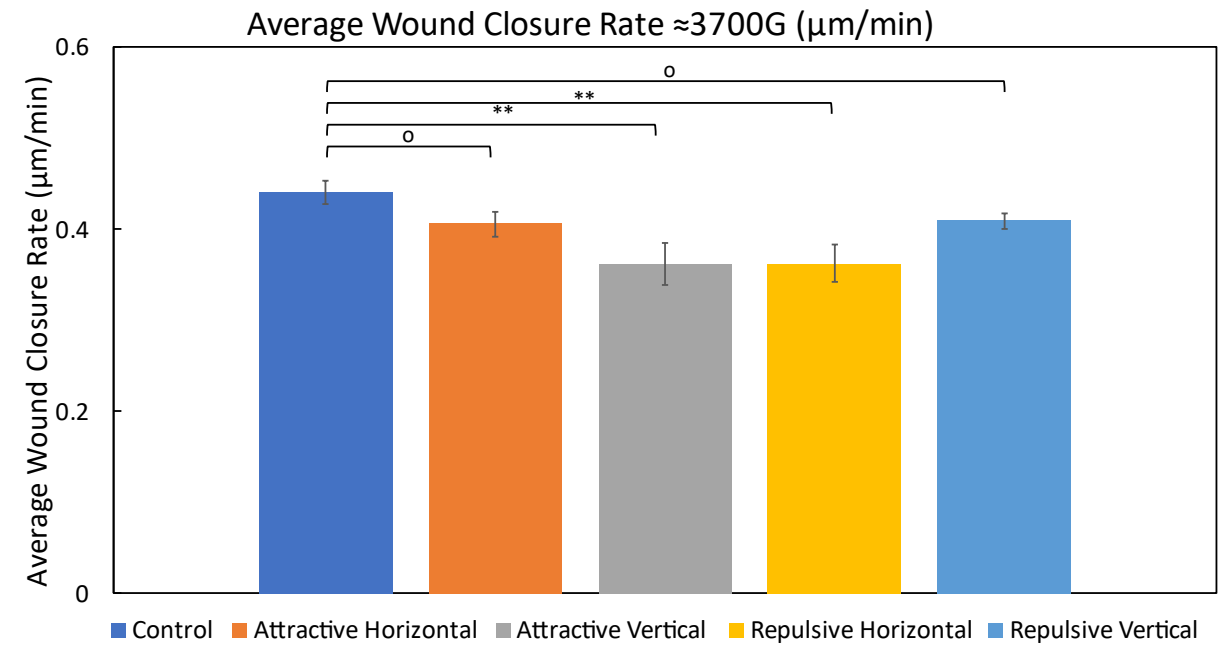

Figure 14: Results average wound closure rate ≈3700 Gauss permanent magnet field.

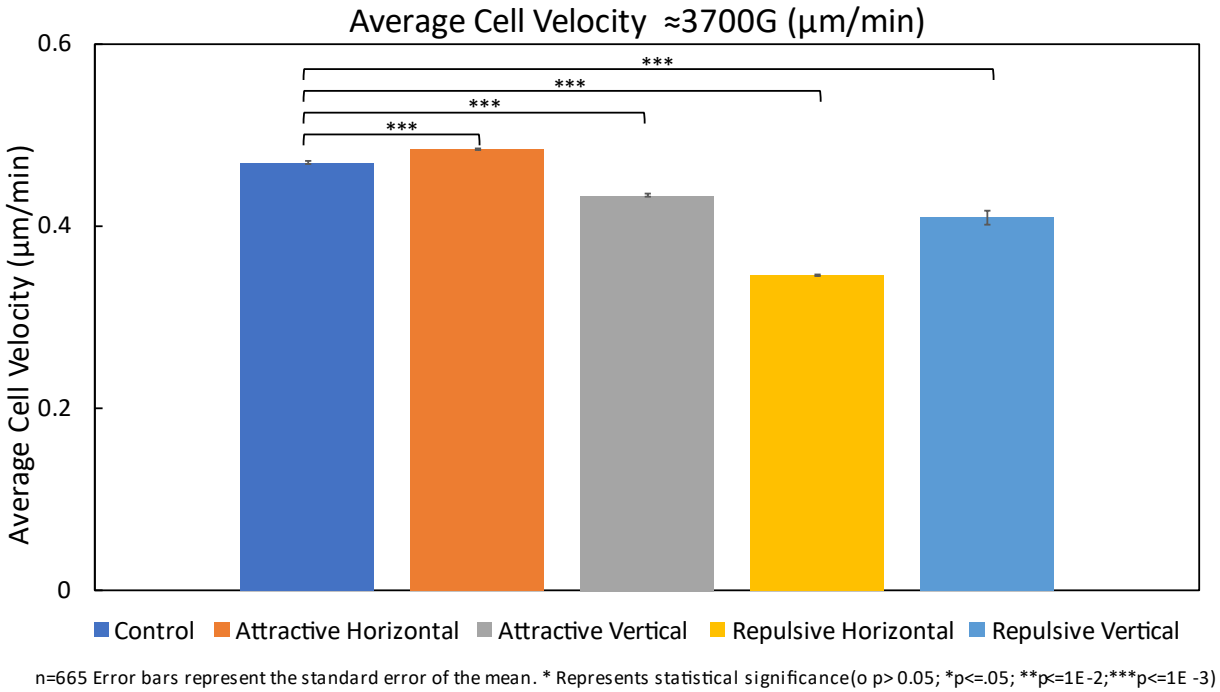

Figure 15: *Results average cell velocity ≈3700 Gauss permanent magnet field.*

Table 7: Table Of wound closure rates and average cell velocity results with significance at ≈1152 Gauss permanent magnet field.

Table Of Wound Closure Rates and Average Cell Velocity Results With Significance at ≈1152G

Measurement	Control	Attractive Horizontal	Attractive Vertical	Repulsive Horizontal	Repulsive Vertical
Average Closure Rate (µm/m)	.3359±.0273	.2813±.0180	.2929±.0170	.3042±.0306	.2900±.01667
Percent Difference		-16%	-13%	-9%	-14%
Significance		Not Significant	Not Significant	Not Significant	Not Significant
Average Cell Velocity (µm/m)	.4771±.0018	.4744±.0010	.3844±.0010	.4106±.0014	.4338±.0022
Percent Difference		-1%	-19%	-13%	-9%
Significance		Not Significant	Significant	Significant	Significant

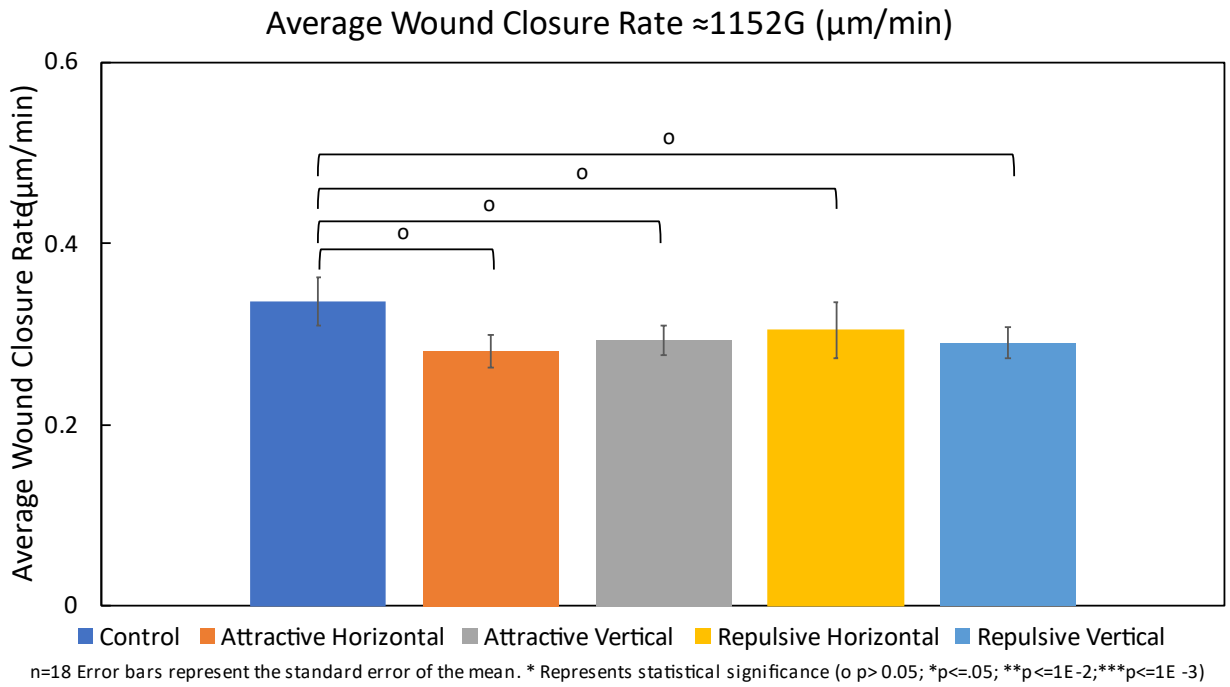

n=18 Error bars represent the standard error of the mean. * Represents statistical significance (o p> 0.05; *p<=.05; **p<=1E-2;***p<=1E -3)

Figure 16: Results average wound closure rate ≈1152 Gauss permanent magnet field.

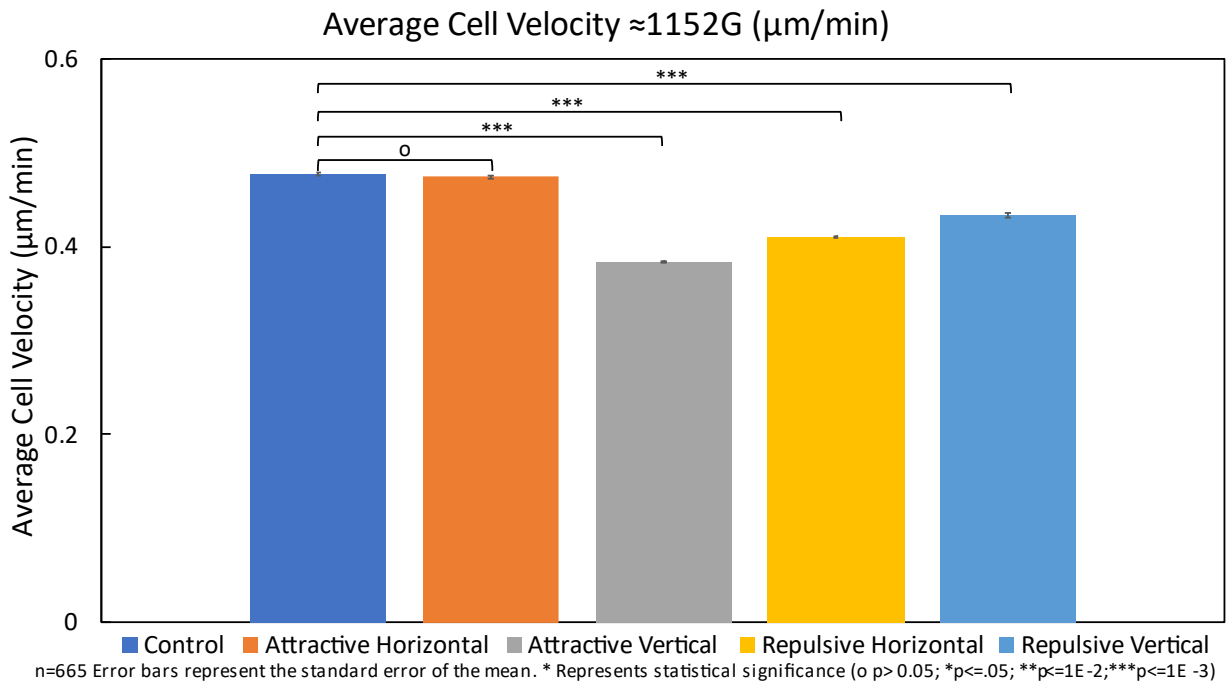

Figure 17: Results average cell velocity ≈1152 Gauss permanent magnet field.

Table 8: *Table Of wound closure rates and average cell velocity results with significance at ≈650 Gauss permanent magnet field.*

Table Of Wound Closure Rates and Average Cell Velocity Results With Significance at ≈650G

Measurement	Control	Attractive Horizontal	Attractive Vertical	Repulsive Horizontal	Repulsive Vertical
Average Closure Rate (µm/m)	0.5643±.0122	0.3668±.0118	0.4312±.0084	0.31225±.0118	0.3972±.0161
Percent Difference		-35%	-24%	-45%	-30%
Significance		Significant	Significant	Significant	Significant
Average Cell Velocity (µm/m)	0.5840±.0023	0.4658±.0017	0.4540±.0010	0.4590±.0018	0.5325±.0011
Percent Difference		-20%	-22%	-21%	-8%
Significance		Significant	Significant	Significant	Significant

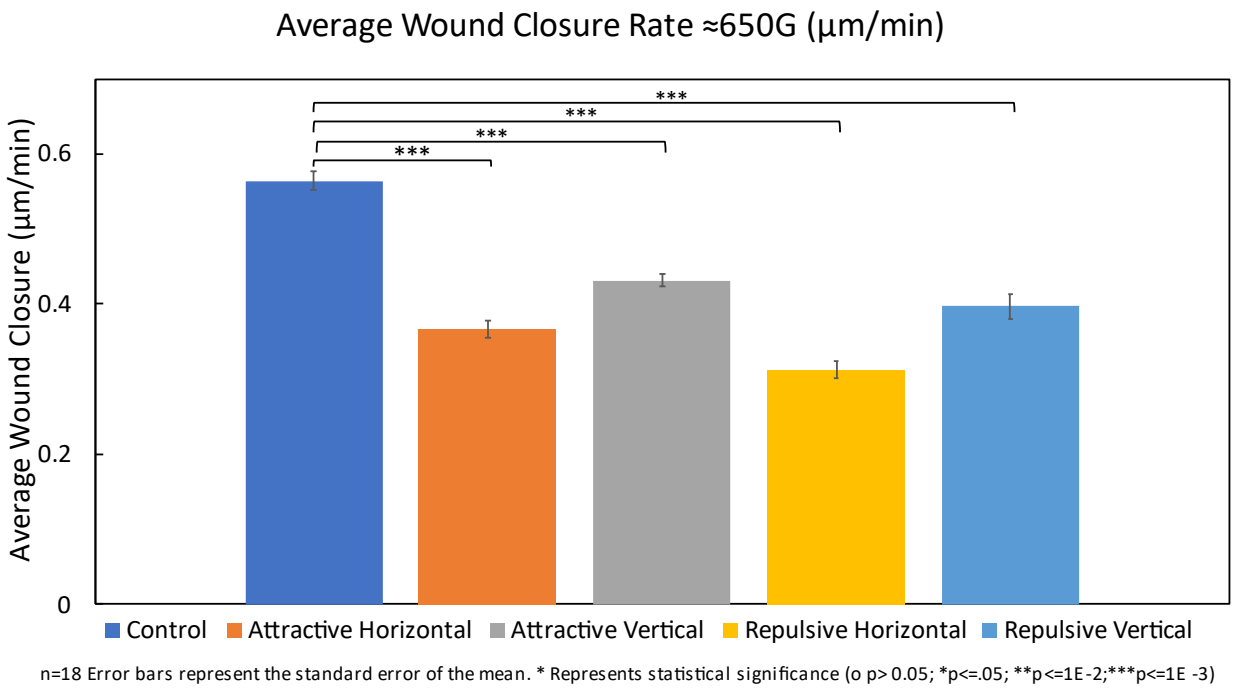

Figure 18: Results average wound closure rate ≈650 Gauss permanent magnet field.

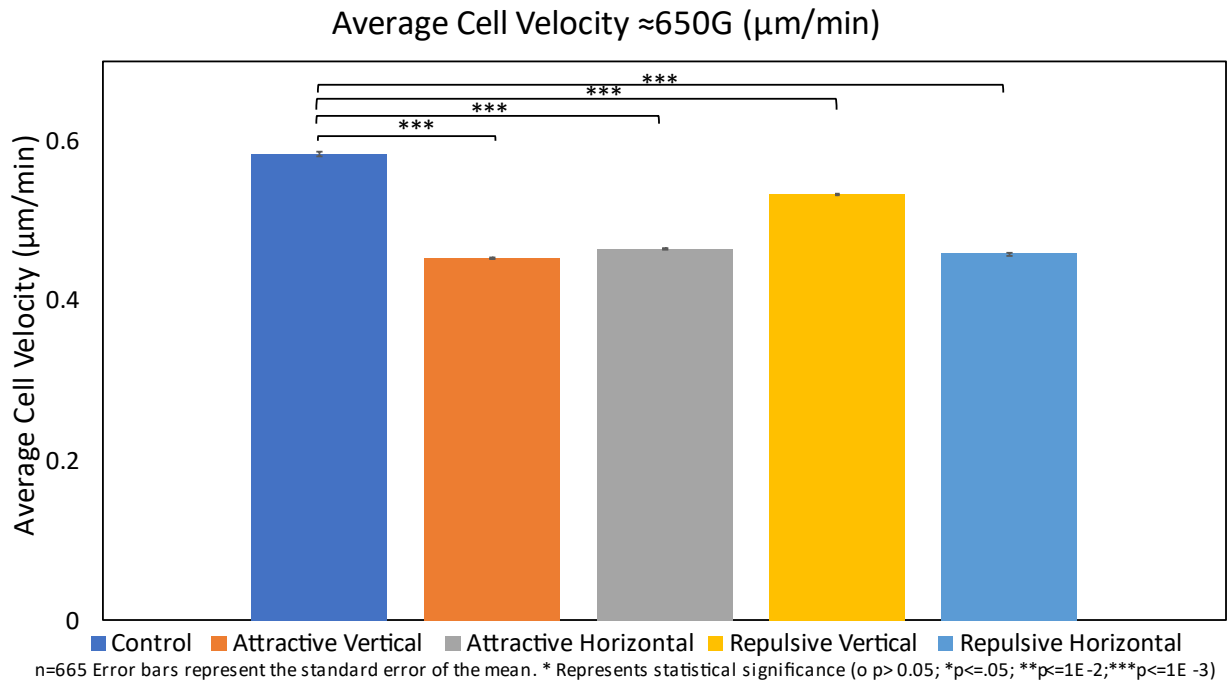

Figure 19: Results average cell velocity ≈650 Gauss permanent magnet field.

Table 9: *Table Of wound closure rates and average cell velocity results with significance at 50 Gauss galvanometer field.*

Table Of Wound Closure Rates and Average Cell Velocity Results With Significance at ≈ 50G

Measurement	Control Group One	Attractive Horizontal	Attractive Vertical	Control Group Two	Repulsive Horizontal	Repulsive Vertical
Average Closure Rate (µm/m)	0.2217±.0121	0.4886±.0233	.5317±.0145	.6067±.0207	.1898±.0060	.2230±.0135
Percent Difference		120%	140%		-69%	-63%
Significance		Significant	Significant		Significant	Significant
Average Cell Velocity (µm/m)	.2947±.0064	.5410±.0016	5858±.0009	.6492±.0021	.2995±.0018	.3019±.0015
Percent Difference		84%	98%		-54%	-53%
Significance		Significant	Significant		Significant	Significant

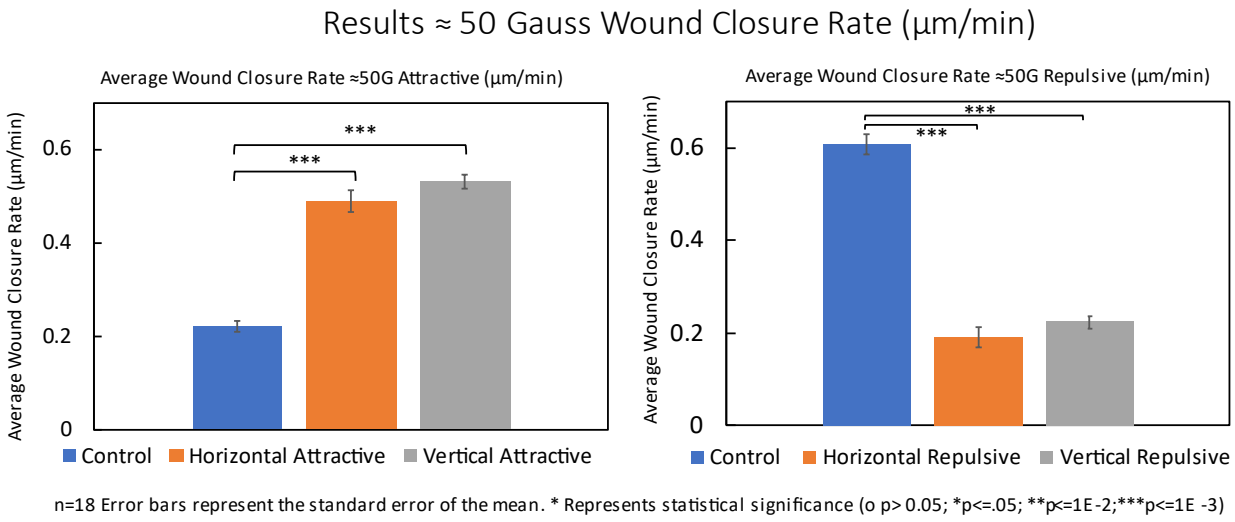

Figure 20: Results average wound closure rate 50 Gauss galvanometer field.

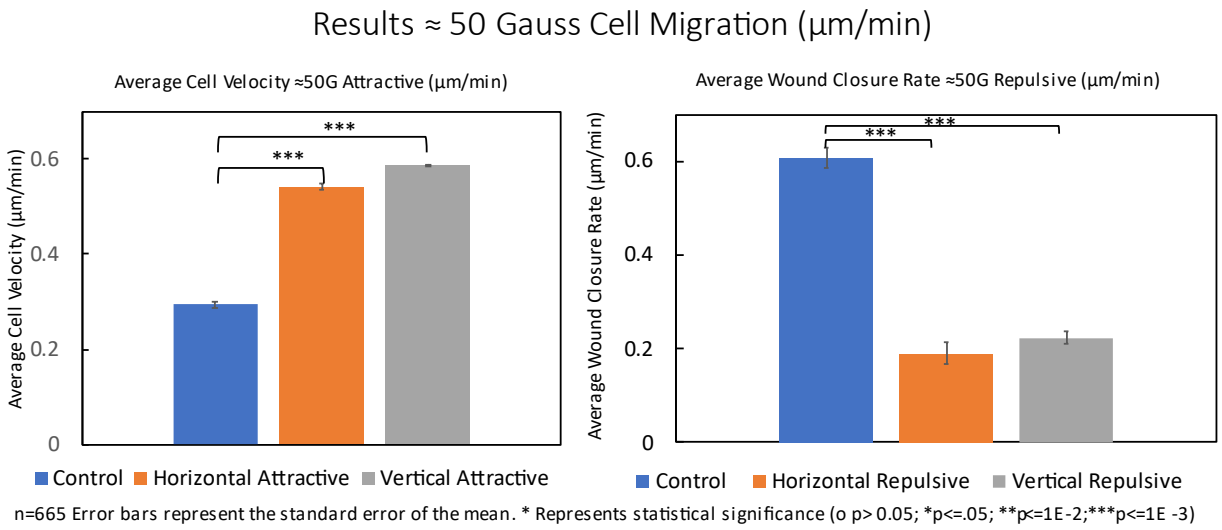

Figure 21: Results average cell velocity 50 Gauss galvanometer field.

Table 10: *Table Of wound closure rates and average cell velocity results with significance under 100mv/mm electrical stimulation.*

Table Of Wound Closure Rates and Average Cell Velocity Results With Significance at 100 mv/mm

Measurement	Control Group One	Horizontal	Control Group Two	Vertical
Average Closure Rate (µm/m)	.7336±.0232	.9023±.0500	.4060±.0310	.4527±.0341
Percent Difference		23%		11%
Significance		Significant		Not Significant
Average Cell Velocity (µm/m)	0.9982±.0062	1.1158±.0052	1.2790±.0090	1.416±.0098
Percent Difference		12%		11%
Significance		Significnt		Significant

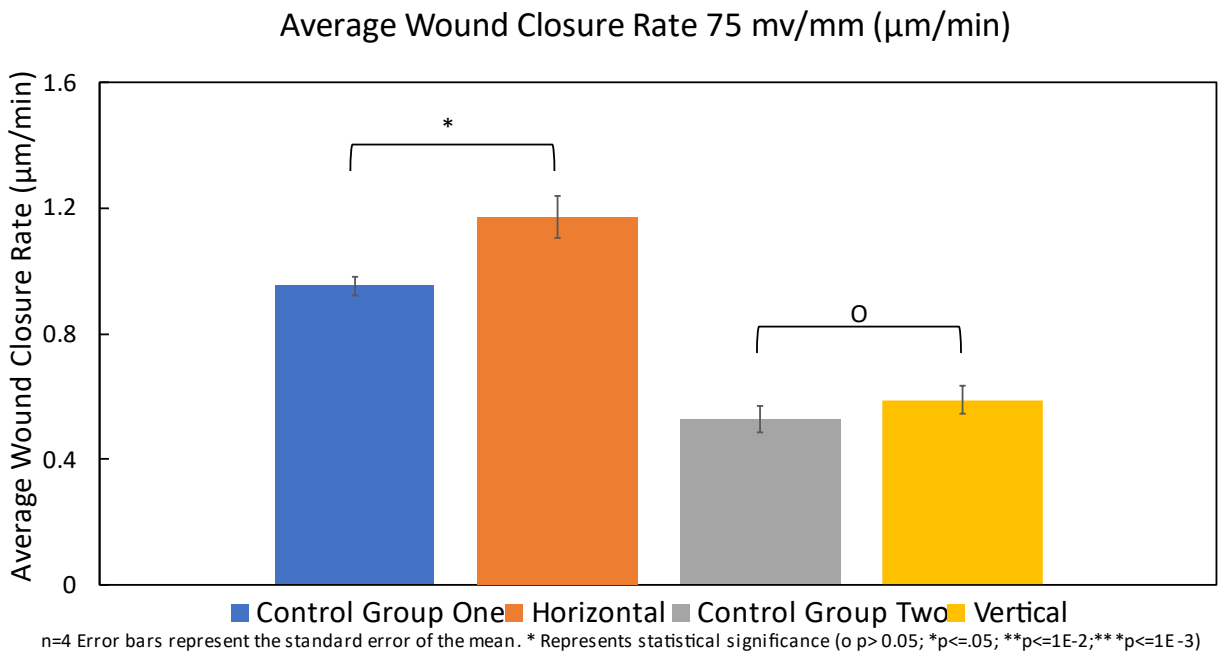

Figure 22: *Results average wound closure under 75mv/mm electrical stimulation.*

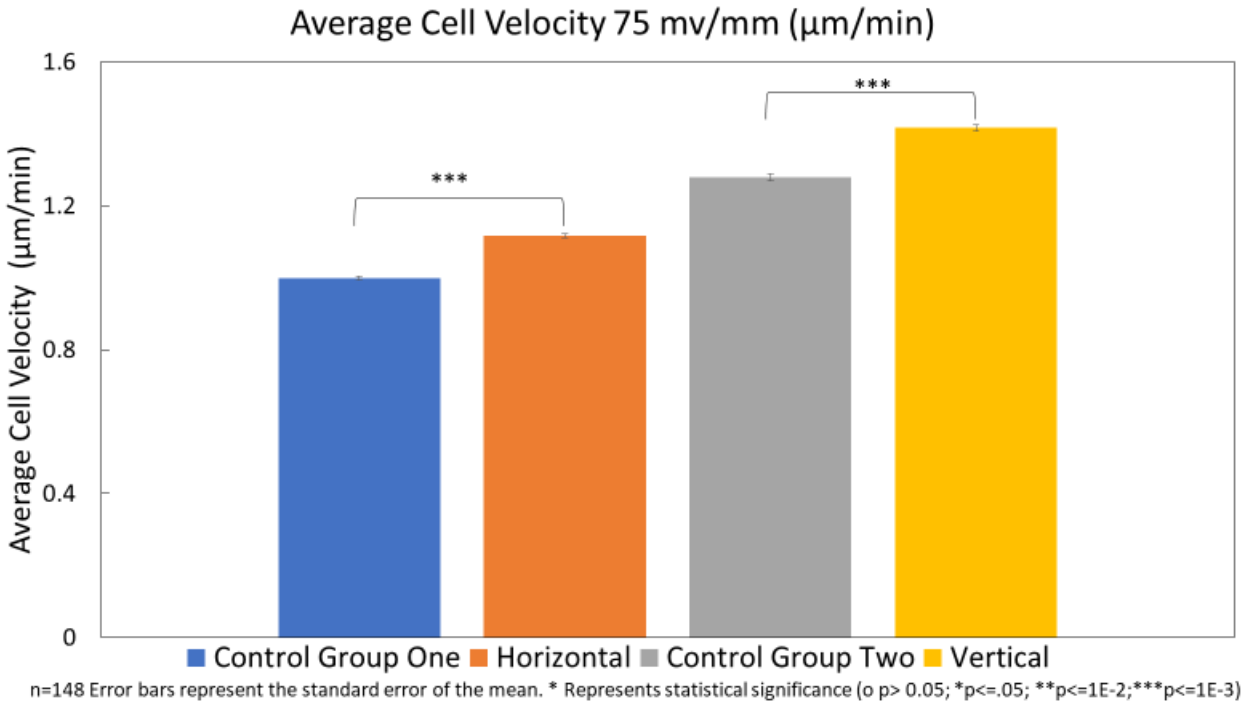

Figure 23: *Results average cell velocity under 75mv/mm electrical stimulation.*

Discussion and Conclusions

Both magnetic and electrical therapies show promise under specific conditions. A wound orientation that is perpendicular to the electoral or magnetic field seems to produce the best results for wound-healing applications. For magnetic stimulation low magnetic field strength of around 50G seems to be necessary for positive wound healing outcomes. In addition, magnetic therapies in the 650G have the potential for use as an antiangiogenic therapy with a significant decrease in both wound closure rates and average cell velocity. This has applications in controlling the growth of cancerous masses. Electrical stimulation also shows promise in improving wound healing rates as a low voltage device providing stimulation of 75mv/mm proved effective in increasing wound closure rates. Further research could be done to optimize the stimulation voltage and magnetic field strength for wound-healing. And determining the best magnetic field strength to inhibit endothelial migration and wound-healing for antiangiogenic applications.

Supplementary

For attractive and repulsive conditions magnets were used in either constructive or interfering magnet positions respectively to determine if orientation and field pattern influence wound-healing behavior.

Figure 24:*Visualization of magnetic field lines relative to 12 well dish positions. Left) Repulsive. Right) Attractive*

For the permanent magnet field study magnets were placed along the long edge of the 12-well dish underneath the microscope's stages cell gas chamber.

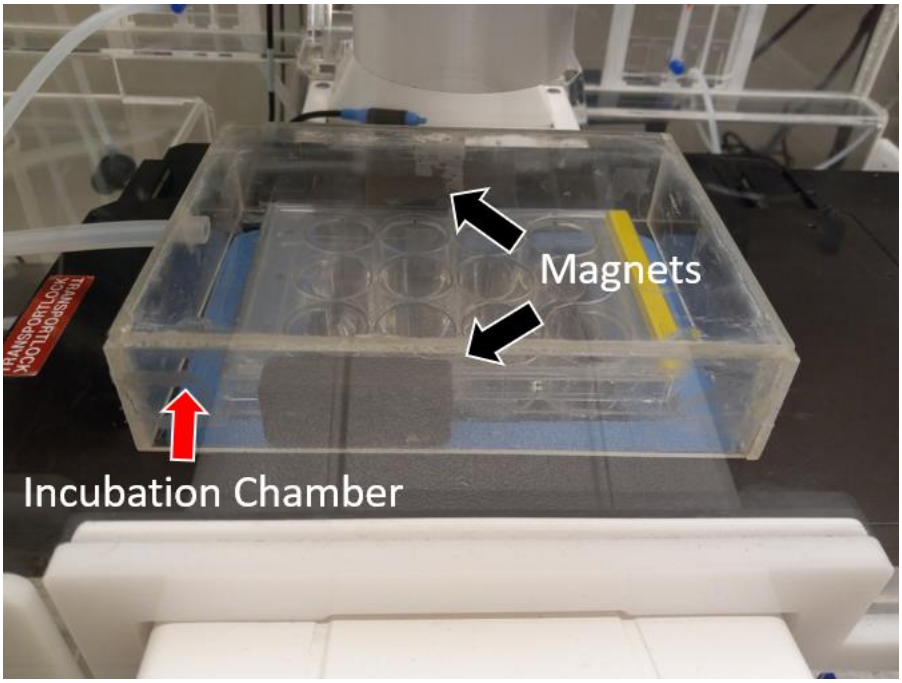

Figure 25: Permanent magnet experimental setup on the microscope stage.

For the galvanometer study, two tangent field galvanometers hooked up to a power supply were used to generate a 50G magnetic field that was calibrated using a Gauss meter and placed within the temperature-controlled microscope stage for imaging.

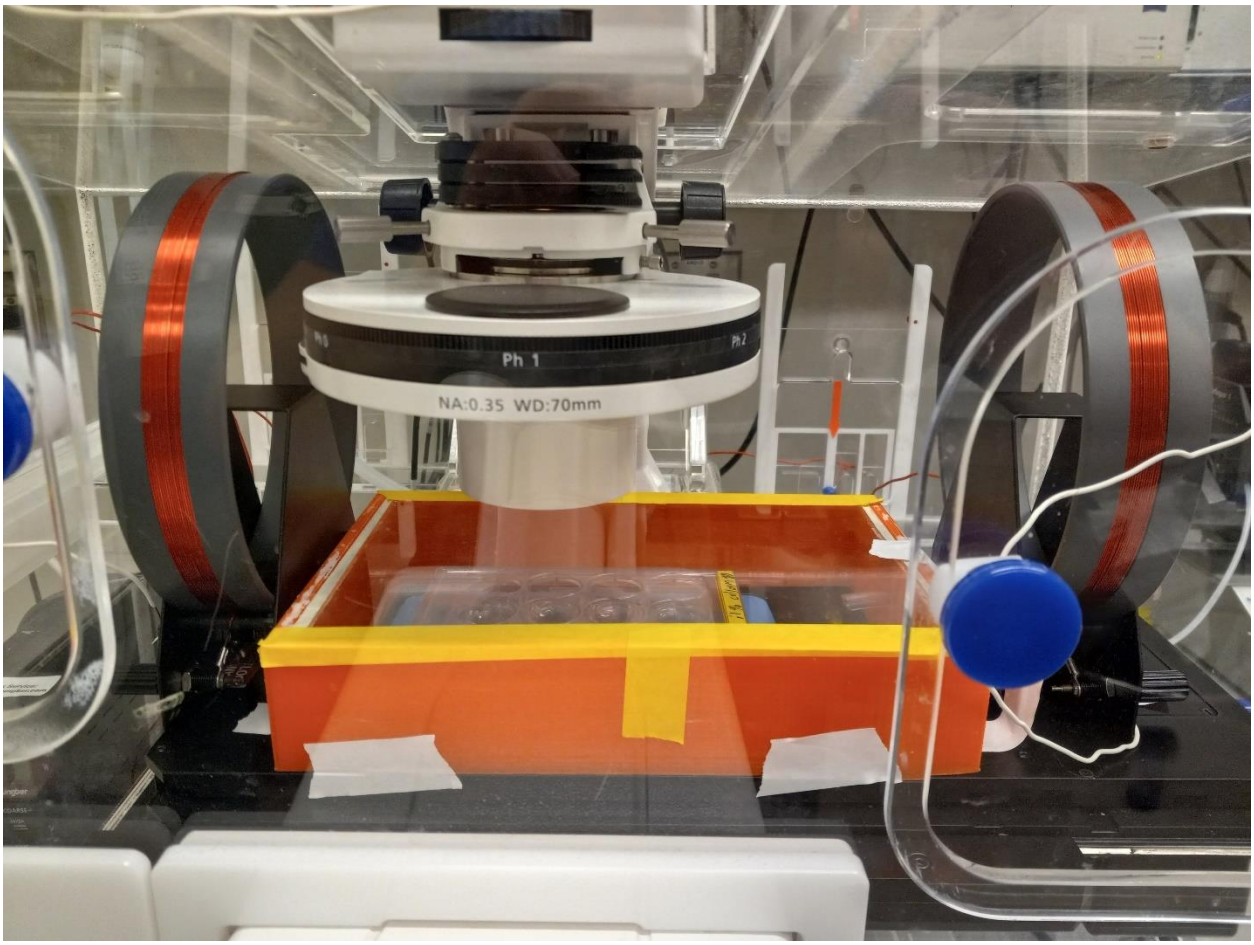

Figure 26: Tangent Field galvanometer experimental setup on the microscope stage.

For the scratch tests wounds were made with either a vertical or horizontal orientation with respect to the microscope camera and corresponded to perpendicular and parallel to the face of the magnet respectively to the face of the permanent magnet. For the galvanometer, the orientation of the magnetic field was 90° offset compared to the permanent magnets.

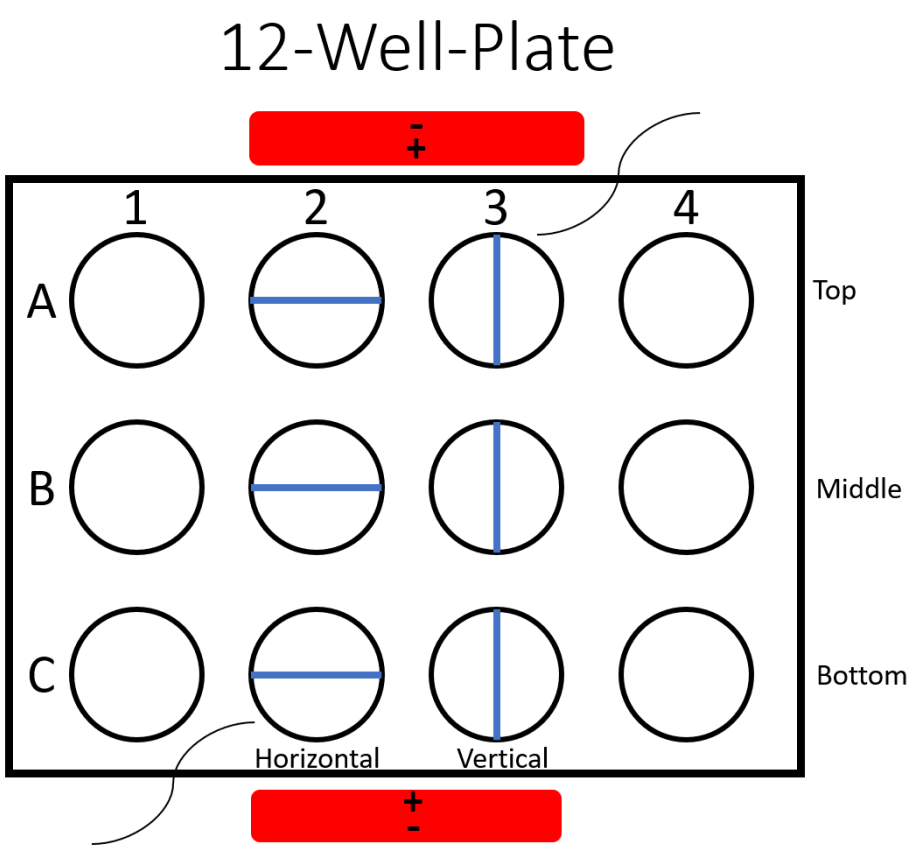

Figure 27: Orientation of a repulsive magnet scratch test with horizontal and vertical wound orientations.

The electrical stimulation setup was composed of an Arduino based wave form generator. An oscilloscope to monitor voltage output and a cell stimulation chamber. The cell culture chamber is composed of glass bottom cell culture dish with a lid designed for the insertion of two pure zinc wire nodes.

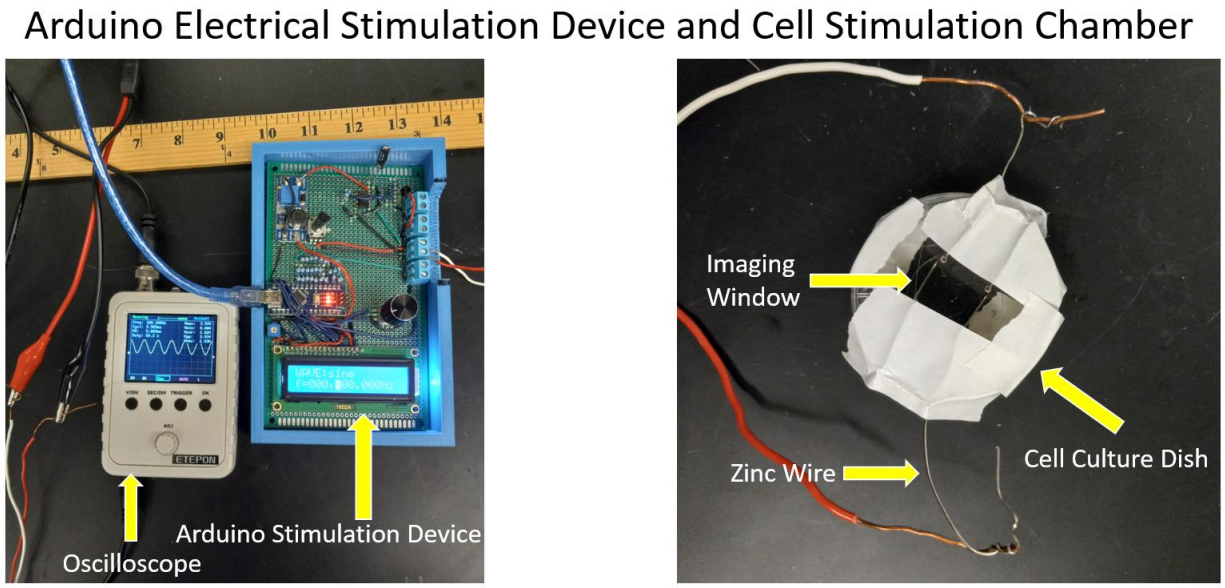

Figure 28: Components of the electrical stimulation setup

The Arduino waveform generator was fabricated for use in this set of experiments. This solution was chosen for its low cost and ready availability along with supporting open source[100].

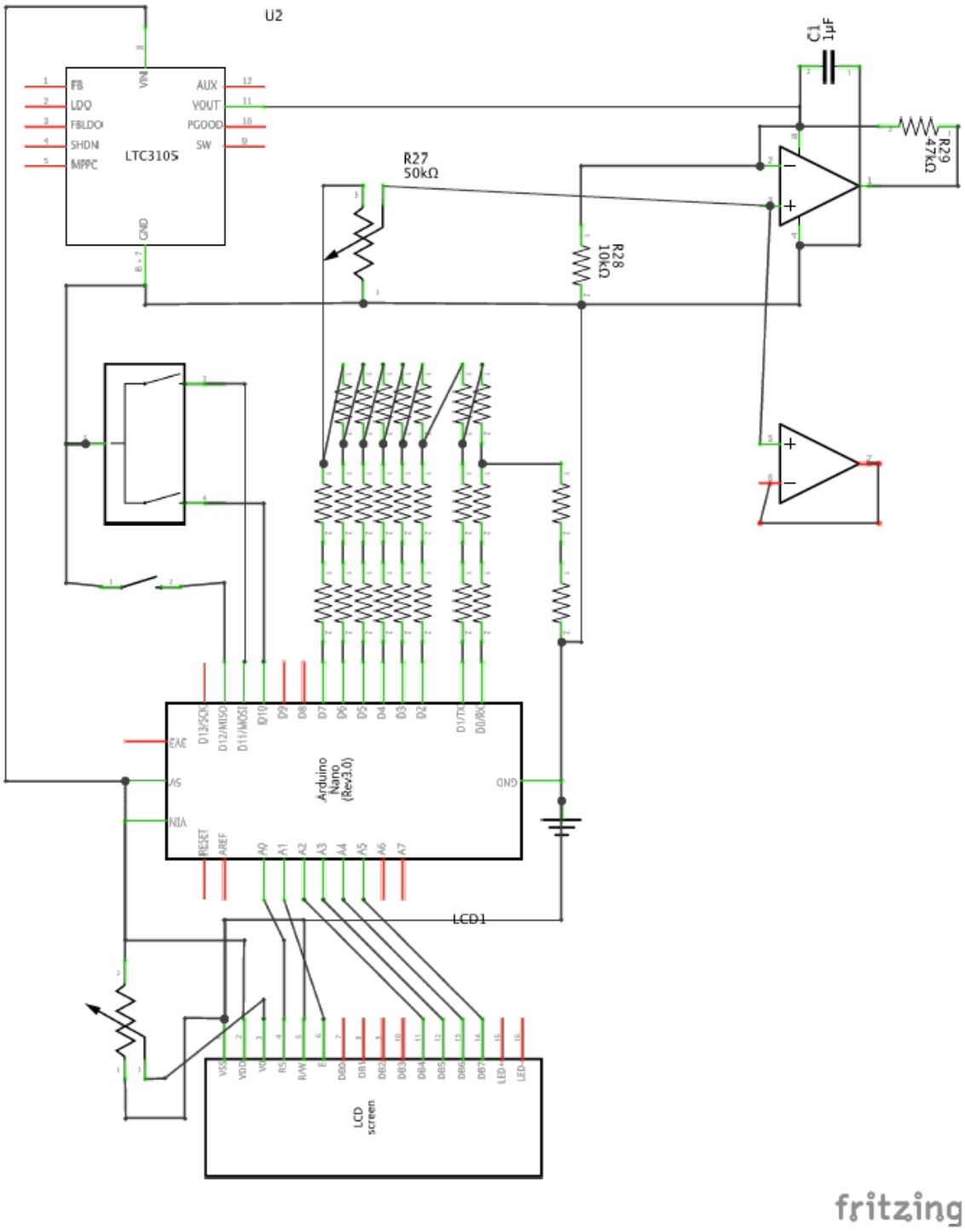

Figure 29: Schematic for the Arduino waveform generator [100]

Electrical stimulation was performed with the wound positioned between two zinc wire nodes to provide electrical stimulation in the below arrangements.

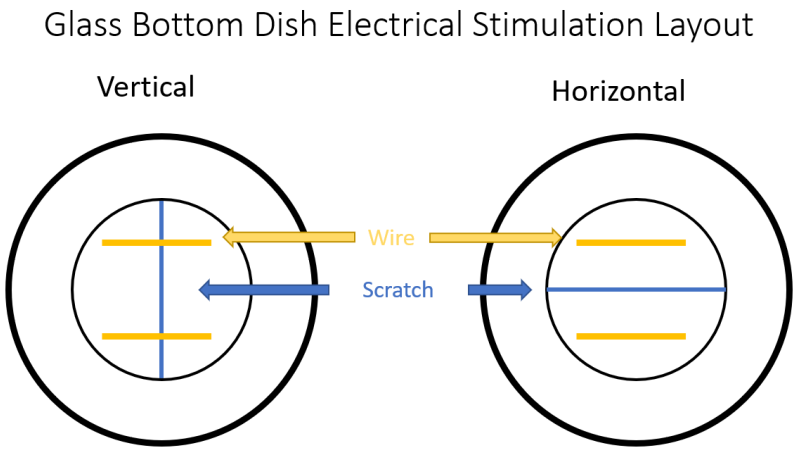

Figure 30: Orientation of an electrical stimulation experiment scratch test with horizontal and vertical wound orientations.

For measuring the width of the wound Fiji was used to measure the width of the wound space using the cameras pixel to micron conversion factor within its measurement tools. From this, the rectangular measurement tool was used to measure the average wound width through the wound-healing process.

Figure 31: *Wound width measurement via measurement tool within Fiji.*

CHAPTER SIX: BROADER IMPACTS

Characterizing Barrier Disruption

By looking at the characteristics of cell mechanics associated with the targeting of specific cell-cell junctions we can see that cell-substate tractions increased for every type of junction tested. However, the impact on average normal stress and maximum shear stresses can vary from one pharmaceutical disruptor to another. This is important as it shows that cells do not mechanically behave the same for each type of barrier disruption and may be dosage and exposure dependent. Looking at the specific types of junctions that were disrupted allows us to compare other drugs and diseases that are known to disrupt these cell-cell junctions and be used as a tool the help characterize and predict the associated cell mechanics.

Wound-Healing Therapies

With the dramatically improved wound closure and cell migration under the 50G attractive wound-healing conditions. The promise of using weak magnetic stimulation to improve wound-healing rates shows promise. This could improve patient recovery outcomes and provide a low-cost solution to aid in recovery. In addition to this electrical stimulation therapies also appear to be effective provided that the orientation of the simulation is arranged with the wound parallel to the voltage potential.

Cell Migration Inhibition

For almost all other conditions the stronger magnetic fields reduced the wound closure rate and cell migration response. The discovered reduction in wound closure rate and average cell velocity for the other conditions, however, presents another potential application of such magnetic

therapy as an antiangiogenic treatment. This could have supporting applications in cancer treatments using strong magnets in cancerous areas. This could have applications as a supplementary form of anti-angiogenic therapy. Moderately strong magnets around the 650G range could be used as a localized inhibitor of angiogenesis and could be used to supplement other cancer therapies.

CHAPTER SEVEN: FUTURE WORK

Endothelial cells play an important role as part of the cardiovascular system forming the semipermeable membrane that regulates the flow of materials into and out of the blood stream. This function is carried out through cell-cell junctions. These junctions play an important role in also transferring the forces to one another as part of their functions. Looking at characterizing how the disruption of different cell-cell junctions influences the permeability we can confirm that disrupting claudin-5, Cx43, and VE-cadherin junctions can all lead to an increase in paracellular permeability. In addition to this, it is shown that cell substrate tractions significantly increase under all disrupted conditions and may be a reaction to disruption in general. The disruption of Claudin-5 with thrombin and VE-cadherin with histamine and Thapsigargin caused a decrease in the average normal intercellular stress within the monolayer. A moderate decrease in maximum intercellular shear stress was found when disrupting with histamine that causes barrier disruption by putting tension on adherens junctions via the actin filaments and thrombin. Chalcone and thapsigargin disruption however saw an increase in maximum shear stress. This shows that different types of disruption can influence cell mechanics differently and can be used to characterize the disruption caused by targeting specific cell-cell junctions. Looking at

pathological methods of disruption such as with end glycation products produced in diabetic patents and spike proteins in corona viruses would be pathological endothelial disruptors that would be of great interest to test and compare in the future determining how pathological conditions such as viral spike proteins and diabetic AGE increase permeability and how disease compare to pharmacological disruption mechanical.

Looking at another function that cell mechanics plays an important role in is cell migration. Cell migration is regulated by a stress gradient made by leader cells that start the migration process and recruit other cells to follow via intercellular stresses. This process is vital in wound-healing as endothelial cells need to migrate in the wound space for it to regenerate as part of angiogenesis. In our search to see if magnetic therapies could improve wound-healing, we found that only one pair of magnetic conditions produced a significant improvement in wound closure times. These conditions were with a constructive attractive 50G magnetic field. In addition, the greatest improvement in average cell velocities was also noted for these conditions. For disruptive repulsive 50G magnetic field and all other stronger magnetic conditions wound closure slowed. For the most part, this was also accompanied by a decrease in cell velocity as well. This unexpected result provides a possible opportunity to use stronger magnets, particularly in the range of ≈650G as potentially an anti-angiogenic therapy. The exact Gauss strength for both improved wound-healing and potential anti-angiogenic therapy as well as the best method of administration are both topics of interest for further study. For this the use of an electrical stimulation device administered to endothelial wound at voltages between 50 μv/mm and 100 μv/mm would be tested to determine the most effective voltage along with testing different pulse rates of electrical stimulation.

REFERENCES

[1] • Galkina, E. Ley K ; • Jalkanen, and S. Salmi, "VE-Cadherin," *Arterioscler Thromb Vasc Biol*, vol. 28, no. 2, pp. 223–232, Feb. 2008, doi: 10.1161/ATVBAHA.107.158014.

[2] "Cell Junctions - Molecular Biology of the Cell - NCBI Bookshelf." https://www.ncbi.nlm.nih.gov/books/NBK26857/ (accessed Jul. 25, 2022).

[3] Y. Yang, N. Jamilpour, B. Yao, Z. S. Dean, R. Riahi, and P. K. Wong, "Probing Leader Cells in Endothelial Collective Migration by Plasma Lithography Geometric Confinement," *Scientific Reports 2016 6:1*, vol. 6, no. 1, pp. 1–11, Mar. 2016, doi: 10.1038/srep22707.

[4] A. Le Guelte and J. Gavard, "Role of endothelial cell-cell junctions in endothelial permeability," *Methods in Molecular Biology*, vol. 763, pp. 265–279, 2011, doi: 10.1007/978-1-61779-191-8_18/FIGURES/1_18.

[5] Y. N. Lee, H. I. Yeh, T. Y. Tian, W. W. Lu, Y. S. Ko, and C. H. Tsai, "2',5'-Dihydroxychalcone down-regulates endothelial connexin43 gap junctions and affects MAP kinase activation," *Toxicology*, vol. 179, no. 1–2, pp. 51–60, Sep. 2002, doi: 10.1016/S0300-483X(02)00289-5.

[6] N. Kondo, M. Ogawa, H. Wada, and S. I. Nishikawa, "Thrombin induces rapid disassembly of claudin-5 from the tight junction of endothelial cells," *Exp Cell Res*, vol. 315, no. 17, pp. 2879–2887, Oct. 2009, doi: 10.1016/J.YEXCR.2009.07.031.

[7] R. Sandoval, A. B. Malik, R. D. Minshall, P. Kouklis, C. A. Ellis, and C. Tiruppathi, "Ca2+ signalling and PKCα activate increased endothelial permeability by disassembly of VE—

cadherin junctions," *J Physiol*, vol. 533, no. Pt 2, p. 433, Jun. 2001, doi: 10.1111/J.1469-7793.2001.0433A.X.

[8] D. Kugelmann, L. T. Rotkopf, M. Y. Radeva, A. Garcia-Ponce, E. Walter, and J. Waschke, "Histamine causes endothelial barrier disruption via Ca2+-mediated RhoA activation and tension at adherens junctions," *Scientific Reports 2018 8:1*, vol. 8, no. 1, pp. 1–14, Sep. 2018, doi: 10.1038/s41598-018-31408-3.

[9] A. Kr. Malakar, D. Choudhury, B. Halder, P. Paul, A. Uddin, and S. Chakraborty, "A review on coronary artery disease, its risk factors, and therapeutics," *J Cell Physiol*, vol. 234, no. 10, pp. 16812–16823, Oct. 2019, doi: 10.1002/jcp.28350.

[10] S. Mundi *et al.*, "Endothelial permeability, LDL deposition, and cardiovascular risk factors—a review," *Cardiovasc Res*, vol. 114, no. 1, p. 35, Jan. 2018, doi: 10.1093/CVR/CVX226.

[11] S. Raghavan, D. B. Kenchappa, and M. D. Leo, "SARS-CoV-2 Spike Protein Induces Degradation of Junctional Proteins That Maintain Endothelial Barrier Integrity," *Front Cardiovasc Med*, vol. 0, p. 582, Jun. 2021, doi: 10.3389/FCVM.2021.687783.

[12] C. N. Duong and D. Vestweber, "Mechanisms Ensuring Endothelial Junction Integrity Beyond VE-Cadherin," *Front Physiol*, vol. 11, p. 519, May 2020, doi: 10.3389/FPHYS.2020.00519/BIBTEX.

[13] M. Haberal *et al.*, "Effect of static magnetic field on experimental dermal wound strength," *Indian J Plast Surg*, vol. 45, no. 2, p. 215, May 2012, doi: 10.4103/0970-0358.101281.

[14] G. Thakral, J. LaFontaine, B. Najafi, T. K. Talal, P. Kim, and L. A. Lavery, “Electrical stimulation to accelerate wound healing,” *Diabet Foot Ankle*, vol. 4, Sep. 2013, doi: 10.3402/DFA.V4I0.22081.

[15] N. Raina, R. Rani, and M. Gupta, “Angiogenesis: Aspects in wound healing,” *Endothelial Signaling in Vascular Dysfunction and Disease: From Bench to Bedside*, pp. 77–90, Jan. 2021, doi: 10.1016/B978-0-12-816196-8.00010-2.

[16] M. G. Tonnesen, X. Feng, and R. A. F. Clark, “Angiogenesis in wound healing,” *Journal of Investigative Dermatology Symposium Proceedings*, vol. 5, no. 1, pp. 40–46, 2000, doi: 10.1046/J.1087-0024.2000.00014.X.

[17] G. Cory, “Scratch-wound assay,” *Methods Mol Biol*, vol. 769, pp. 25–30, 2011, doi: 10.1007/978-1-61779-207-6_2.

[18] M. Murrell, P. W. Oakes, M. Lenz, and M. L. Gardel, “Forcing cells into shape: the mechanics of actomyosin contractility,” *Nature Reviews Molecular Cell Biology 2015 16:8*, vol. 16, no. 8, pp. 486–498, Jul. 2015, doi: 10.1038/nrm4012.

[19] A. L. Sieminski, R. P. Hebbel, and K. J. Gooch, “The relative magnitudes of endothelial force generation and matrix stiffness modulate capillary morphogenesis in vitro,” *Exp Cell Res*, vol. 297, no. 2, pp. 574–584, Jul. 2004, doi: 10.1016/j.yexcr.2004.03.035.

[20] A. D. van der Meer, A. A. Poot, J. Feijen, and I. Vermes, “Analyzing shear stress-induced alignment of actin filaments in endothelial cells with a microfluidic assay,” *Biomicrofluidics*, vol. 4, no. 1, p. 011103, Mar. 2010, doi: 10.1063/1.3366720.

[21] A. Munjal and T. Lecuit, “Actomyosin networks and tissue morphogenesis,” *Development*, vol. 141, no. 9, pp. 1789–1793, 2014, doi: 10.1242/dev.091645.

[22] M. Vicente-Manzanares, X. Ma, R. S. Adelstein, and A. R. Horwitz, “Non-muscle myosin II takes centre stage in cell adhesion and migration,” *Nat. Rev. Mol. Cell Biol.*, vol. 10, no. 11, pp. 778–790, Nov. 2009, doi: 10.1038/nrm2786.

[23] B. Ladoux and R. M. Mège, “Mechanobiology of collective cell behaviours,” *Nature Reviews Molecular Cell Biology 2017 18:12*, vol. 18, no. 12, pp. 743–757, Nov. 2017, doi: 10.1038/nrm.2017.98.

[24] F. Twiss *et al.*, “Vinculin-dependent Cadherin mechanosensing regulates efficient epithelial barrier formation,” *Biol Open*, vol. 1, no. 11, pp. 1128–1140, Nov. 2012, doi: 10.1242/BIO.20122428.

[25] K. Ohashi, S. Fujiwara, and K. Mizuno, “Roles of the cytoskeleton, cell adhesion and rho signalling in mechanosensing and mechanotransduction,” *The Journal of Biochemistry*, vol. 161, no. 3, pp. 245–254, Mar. 2017, doi: 10.1093/JB/MVW082.

[26] F. Martino, A. R. Perestrelo, V. Vinarský, S. Pagliari, and G. Forte, “Cellular mechanotransduction: From tension to function,” *Front Physiol*, vol. 9, no. JUL, p. 824, Jul. 2018, doi: 10.3389/FPHYS.2018.00824/BIBTEX.

[27] T. Luo, K. Mohan, P. A. Iglesias, and D. N. Robinson, “Molecular mechanisms of cellular mechanosensing,” *Nature Materials 2013 12:11*, vol. 12, no. 11, pp. 1064–1071, Oct. 2013, doi: 10.1038/nmat3772.

[28] D. Ingber and D. E. Ingber, “Mechanobiology and diseases of mechanotransduction,” *https://doi.org/10.1080/07853890310016333*, vol. 35, no. 8, pp. 564–577, 2009, doi: 10.1080/07853890310016333.

[29] D. Lu and G. S. Kassab, “Role of shear stress and stretch in vascular mechanobiology,” *J R Soc Interface*, vol. 8, no. 63, p. 1379, Oct. 2011, doi: 10.1098/RSIF.2011.0177.

[30] R. Steward, D. Tambe, C. C. Hardin, R. Krishnan, J. J. Fredberg, and J. J. Fredberg, “Fluid shear, intercellular stress, and endothelial cell alignment.,” *Am J Physiol Cell Physiol*, vol. 308, no. 8, pp. C657-64, Apr. 2015, doi: 10.1152/ajpcell.00363.2014.

[31] D. Ulluwishewa, R. C. Anderson, W. C. McNabb, P. J. Moughan, J. M. Wells, and N. C. Roy, “Regulation of Tight Junction Permeability by Intestinal Bacteria and Dietary Components,” *J Nutr*, vol. 141, no. 5, pp. 769–776, May 2011, doi: 10.3945/JN.110.135657.

[32] M. S. Adil, S. P. Narayanan, and P. R. Somanath, “Cell-cell junctions: structure and regulation in physiology and pathology,” *Tissue Barriers*, vol. 9, no. 1, 2021, doi: 10.1080/21688370.2020.1848212.

[33] T. Okamoto and K. Suzuki, “The Role of Gap Junction-Mediated Endothelial Cell–Cell Interaction in the Crosstalk between Inflammation and Blood Coagulation,” *Int J Mol Sci*, vol. 18, no. 11, Nov. 2017, doi: 10.3390/IJMS18112254.

[34] N. Rahimi, “Defenders and challengers of endothelial barrier function,” *Front Immunol*, vol. 8, no. DEC, p. 1847, Dec. 2017, doi: 10.3389/FIMMU.2017.01847/BIBTEX.

[35] T. Okamoto *et al.*, “Gap junction-mediated regulation of endothelial cellular stiffness,” *Scientific Reports 2017 7:1*, vol. 7, no. 1, pp. 1–12, Jul. 2017, doi: 10.1038/s41598-017-06463-x.

[36] D. A. Goodenough and D. L. Paul, “Gap Junctions,” *Cold Spring Harb Perspect Biol*, vol. 1, no. 1, 2009, doi: 10.1101/CSHPERSPECT.A002576.

[37] C. M. Grimsley-Myers *et al.*, “VE-cadherin endocytosis controls vascular integrity and patterning during development,” *Journal of Cell Biology*, vol. 219, no. 5, May 2020, doi: 10.1083/JCB.201909081/151601.

[38] M. Giannotta, M. Trani, and E. Dejana, “VE-cadherin and endothelial adherens junctions: Active guardians of vascular integrity,” *Dev Cell*, vol. 26, no. 5, pp. 441–454, Sep. 2013, doi: 10.1016/J.DEVCEL.2013.08.020.

[39] M. Corada *et al.*, “Vascular endothelial-cadherin is an important determinant of microvascular integrity in vivo,” *Proc Natl Acad Sci U S A*, vol. 96, no. 17, pp. 9815–9820, Aug. 1999, doi: 10.1073/PNAS.96.17.9815/ASSET/2B1256A9-EA24-467D-9D04-69E4C81B6828/ASSETS/GRAPHIC/PQ1794391010.JPEG.

[40] D. Vestweber, “VE-cadherin: the major endothelial adhesion molecule controlling cellular junctions and blood vessel formation,” *Arterioscler Thromb Vasc Biol*, vol. 28, no. 2, pp. 223–232, Feb. 2008, doi: 10.1161/ATVBAHA.107.158014.

[41] B. J. DeOre, K. A. Tran, A. M. Andrews, S. H. Ramirez, and P. A. Galie, “SARS-CoV-2 Spike Protein Disrupts Blood–Brain Barrier Integrity via RhoA Activation,” *Journal of*

Neuroimmune Pharmacology, vol. 16, no. 4, pp. 722–728, Dec. 2021, doi: 10.1007/S11481-021-10029-0/FIGURES/3.

[42] K. Nagasawa *et al.*, "Possible involvement of gap junctions in the barrier function of tight junctions of brain and lung endothelial cells," *J Cell Physiol*, vol. 208, no. 1, pp. 123–132, Jul. 2006, doi: 10.1002/JCP.20647.

[43] M. M. Islam and R. L. Steward, "Probing Endothelial Cell Mechanics through Connexin 43 Disruption," *Exp Mech*, vol. 59, no. 3, pp. 327–336, Mar. 2019, doi: 10.1007/S11340-018-00445-4.

[44] C. Hardin *et al.*, "Glassy dynamics, cell mechanics, and endothelial permeability," *Journal of Physical Chemistry B*, vol. 117, no. 42, pp. 12850–12856, Oct. 2013, doi: 10.1021/jp4020965.

[45] C. M. Mikelis *et al.*, "RhoA and ROCK mediate histamine-induced vascular leakage and anaphylactic shock," *Nature Communications 2015 6:1*, vol. 6, no. 1, pp. 1–11, Apr. 2015, doi: 10.1038/ncomms7725.

[46] C. C. Hardin *et al.*, "Long-range stress transmission guides endothelial gap formation," *Biochem Biophys Res Commun*, vol. 495, no. 1, pp. 749–754, Jan. 2018, doi: 10.1016/j.bbrc.2017.11.066.

[47] M. J. Rabiet, J. L. Plantier, Y. Rival, Y. Genoux, M. G. Lampugnani, and E. Dejana, "Thrombin-induced increase in endothelial permeability is associated with changes in cell-to-cell

junction organization," *Arterioscler Thromb Vasc Biol*, vol. 16, no. 3, pp. 488–496, 1996, doi: 10.1161/01.ATV.16.3.488.

[48] O. Dubrovskyi, A. A. Birukova, and K. G. Birukov, "Measurement of local permeability at subcellular level in cell models of agonist- and ventilator-induced lung injury.," *Lab Invest*, vol. 93, no. 2, pp. 254–63, Feb. 2013, doi: 10.1038/labinvest.2012.159.

[49] G. L. Bratthauer, "The avidin-biotin complex (ABC) method and other avidin-biotin binding methods.," *Methods Mol Biol*, vol. 588, pp. 257–270, 2010, doi: 10.1007/978-1-59745-324-0_26/FIGURES/3_26.

[50] M. Wilchek and E. A. Bayer, "The avidin-biotin complex in bioanalytical applications," *Anal Biochem*, vol. 171, no. 1, pp. 1–32, May 1988, doi: 10.1016/0003-2697(88)90120-0.

[51] A. Mortensen, L. Cherrier, and R. Walia, "Effect of pirfenidone on wound healing in lung transplant patients," *Multidiscip Respir Med*, vol. 13, no. 1, p. 16, Dec. 2018, doi: 10.1186/s40248-018-0129-4.

[52] M. Rodrigues, N. Kosaric, C. A. Bonham, and G. C. Gurtner, "Wound Healing: A Cellular Perspective," *Physiol Rev*, vol. 99, pp. 665–706, 2019, doi: 10.1152/physrev.00067.2017.-Wound.

[53] D. T. Tambe *et al.*, "Collective cell guidance by cooperative intercellular forces Supporting Online Material," *Nat Mater*, vol. 10, no. 6, pp. 469–475, 2011, doi: 10.1038/nmat3025.

[54] X. Trepat *et al.*, "Physical forces during collective cell migration," *Nat Phys*, vol. 5, no. 6, pp. 426–430, May 2009, doi: 10.1038/nphys1269.

[55] D. T. Tambe *et al.*, “ONLINE SUPPORTING INFORMATION Monolayer Stress Microscopy: limitations, artifacts, and accuracy of recovered intercellular stresses,” pp. 1–17, 2013, [Online]. Available: https://s3-eu-west-1.amazonaws.com/pstorage-plos-3567654/975194/File_S1.pdf

[56] S. Hamdan *et al.*, “Nanotechnology-Driven Therapeutic Interventions in Wound Healing: Potential Uses and Applications,” *ACS Cent Sci*, vol. 3, no. 3, pp. 163–175, Mar. 2017, doi: 10.1021/ACSCENTSCI.6B00371/ASSET/IMAGES/LARGE/OC-2016-003714_0006.JPEG.

[57] H. A. R. Hadi and J. Al Suwaidi, “Endothelial dysfunction in diabetes mellitus.,” *Vasc Health Risk Manag*, vol. 3, no. 6, pp. 853–76, 2007.

[58] S. L. Henry, M. J. Concannon, and G. J. Yee, “The Effect of Magnetic Fields on Wound Healing: Experimental Study and Review of the Literature,” *Eplasty*, vol. 8, p. e40, Jul. 2008, Accessed: Jul. 18, 2022. [Online]. Available: /pmc/articles/PMC2490801/

[59] J. Zhao, Y. G. Li, K. Q. Deng, P. Yun, and T. Gong, “Therapeutic Effects of Static Magnetic Field on Wound Healing in Diabetic Rats,” *J Diabetes Res*, vol. 2017, 2017, doi: 10.1155/2017/6305370.

[60] M. Pooam, B. Aguida, S. Drahy, N. Jourdan, and M. Ahmad, “Therapeutic application of light and electromagnetic fields to reduce hyper-inflammation triggered by COVID-19,” *Commun Integr Biol*, vol. 14, no. 1, pp. 66–77, 2021, doi: 10.1080/19420889.2021.1911413.

[61] S.-E. Kwak, J.-H. Lee, D. Zhang, and W. Song, “Angiogenesis: focusing on the effects of exercise in aging and cancer,” *J Exerc Nutrition Biochem*, vol. 22, no. 3, p. 21, Sep. 2018, doi: 10.20463/JENB.2018.0020.

[62] Z. Ungvari *et al.*, “Endothelial dysfunction and angiogenesis impairment in the ageing vasculature,” *Nat Rev Cardiol*, vol. 15, no. 9, pp. 555–565, Sep. 2018, doi: 10.1038/S41569-018-0030-Z.

[63] D. Hanahan and R. A. Weinberg, “Hallmarks of cancer: The next generation,” *Cell*, vol. 144, no. 5, pp. 646–674, Mar. 2011, doi: 10.1016/J.CELL.2011.02.013.

[64] P. Vafopoulou and M. Kourti, “Anti-angiogenic drugs in cancer therapeutics: a review of the latest preclinical and clinical studies of anti-angiogenic agents with anticancer potential,” *J Cancer Metastasis Treat*, vol. 8, p. 18, May 2022, doi: 10.20517/2394-4722.2022.08.

[65] S. Yonucu, D. Yılmaz, C. Phipps, M. B. Unlu, and M. Kohandel, “Quantifying the effects of antiangiogenic and chemotherapy drug combinations on drug delivery and treatment efficacy,” *PLoS Comput Biol*, vol. 13, no. 9, p. e1005724, Sep. 2017, doi: 10.1371/JOURNAL.PCBI.1005724.

[66] G. Des Guetz, B. Uzzan, K. Chouahnia, and J. F. Morère, “Cardiovascular toxicity of anti-angiogenic drugs,” *Target Oncol*, vol. 6, no. 4, pp. 197–202, Dec. 2011, doi: 10.1007/S11523-011-0204-7/METRICS.

[67] P. Efentakis *et al.*, “Myocardial Protection and Current Cancer Therapy: Two Opposite Targets with Inevitable Cost,” *Int J Mol Sci*, vol. 23, no. 22, Nov. 2022, doi: 10.3390/IJMS232214121.

[68] A. S. Oguntade, F. Al-Amodi, A. Alrumayh, M. Alobaida, and M. Bwalya, “Anti-angiogenesis in cancer therapeutics: the magic bullet,” *J Egypt Natl Canc Inst*, vol. 33, no. 1, pp. 1–11, Dec. 2021, doi: 10.1186/S43046-021-00072-6/TABLES/2.

[69] R. I. Teleanu, C. Chircov, A. M. Grumezescu, and D. M. Teleanu, “Tumor Angiogenesis and Anti-Angiogenic Strategies for Cancer Treatment,” *Journal of Clinical Medicine 2020, Vol. 9, Page 84*, vol. 9, no. 1, p. 84, Dec. 2019, doi: 10.3390/JCM9010084.

[70] B. Al-Husein, M. Abdalla, M. Trepte, D. L. DeRemer, and P. R. Somanath, “Anti-angiogenic therapy for cancer: An update,” *Pharmacotherapy*, vol. 32, no. 12, p. 1095, Dec. 2012, doi: 10.1002/PHAR.1147.

[71] N. S. Vasudev and A. R. Reynolds, “Anti-angiogenic therapy for cancer: current progress, unresolved questions and future directions,” *Angiogenesis*, vol. 17, no. 3, p. 471, 2014, doi: 10.1007/S10456-014-9420-Y.

[72] Y. Lei *et al.*, “SARS-CoV-2 Spike Protein Impairs Endothelial Function via Downregulation of ACE 2,” *Circ Res*, vol. 128, no. 9, pp. 1323–1326, Apr. 2021, doi: 10.1161/CIRCRESAHA.121.318902.

[73] G. Gallo, M. Volpe, and C. Savoia, “Endothelial Dysfunction in Hypertension: Current Concepts and Clinical Implications,” *Front Med (Lausanne)*, vol. 8, p. 3022, Jan. 2022, doi: 10.3389/FMED.2021.798958/BIBTEX.

[74] D. Konukoglu and H. Uzun, “Endothelial dysfunction and hypertension,” *Adv Exp Med Biol*, vol. 956, pp. 511–540, Dec. 2016, doi: 10.1007/5584_2016_90/FIGURES/12.

[75] R. P. Brandes, “Endothelial Dysfunction and Hypertension,” *Hypertension*, vol. 64, no. 5, pp. 924–928, Nov. 2014, doi: 10.1161/HYPERTENSIONAHA.114.03575.

[76] S. R. Caliari and J. A. Burdick, “A practical guide to hydrogels for cell culture,” 2016. doi: 10.1038/nmeth.3839.

[77] F. S. Pasqualini, A. Agarwal, B. B. O’Connor, Q. Liu, S. P. Sheehy, and K. K. Parker, “Traction force microscopy of engineered cardiac tissues,” *PLoS One*, vol. 13, no. 3, Mar. 2018, doi: 10.1371/journal.pone.0194706.

[78] T. Oliver, K. Jacobson, and M. Dembo, “Design and use of substrata to measure traction forces exerted by cultured cells.,” *Methods Enzymol*, vol. 298, pp. 497–521, 1998, Accessed: Mar. 19, 2019. [Online]. Available: http://www.ncbi.nlm.nih.gov/pubmed/9751905

[79] J. P. Butler, I. M. Tolic-Norrelykke, B. Fabry, and J. J. Fredberg, “Traction fields, moments, and strain energy that cells exert on their surroundings,” *AJP: Cell Physiology*, vol. 282, no. 3, pp. C595–C605, 2002, doi: 10.1152/ajpcell.00270.2001.

[80] D. T. Tambe *et al.*, “Monolayer Stress Microscopy: Limitations, Artifacts, and Accuracy of Recovered Intercellular Stresses,” *PLoS One*, vol. 8, no. 2, 2013, doi: 10.1371/journal.pone.0055172.

[81] T. S. Frost, L. Jiang, R. M. Lynch, and Y. Zohar, “Permeability of Epithelial/Endothelial Barriers in Transwells and Microfluidic Bilayer Devices,” *Micromachines (Basel)*, vol. 10, no. 8, Aug. 2019, doi: 10.3390/MI10080533.

[82] D. A. Antonetti, E. Lieth, A. J. Barber, and T. W. Gardner, “Molecular mechanisms of vascular permeability in diabetic retinopathy,” *Semin Ophthalmol*, vol. 14, no. 4, pp. 240–248, 1999, doi: 10.3109/08820539909069543.

[83] Y. Ni, T. Teng, R. Li, A. Simonyi, G. Y. Sun, and J. C. Lee, “TNFα alters occludin and cerebral endothelial permeability: Role of p38MAPK,” *PLoS One*, vol. 12, no. 2, p. e0170346, Feb. 2017, doi: 10.1371/journal.pone.0170346.

[84] A. Hartsock and W. J. Nelson, “Adherens and tight junctions: Structure, function and connections to the actin cytoskeleton,” *Biochimica et Biophysica Acta (BBA) - Biomembranes*, vol. 1778, no. 3, pp. 660–669, Mar. 2008, doi: 10.1016/j.bbamem.2007.07.012.

[85] C. Greene, N. Hanley, and M. Campbell, “Claudin-5: gatekeeper of neurological function,” *Fluids and Barriers of the CNS 2019 16:1*, vol. 16, no. 1, pp. 1–15, Jan. 2019, doi: 10.1186/S12987-019-0123-Z.

[86] W. Jia, R. Lu, T. A. Martin, and W. G. Jiang, “The role of claudin-5 in blood-brain barrier (BBB) and brain metastases (Review),” *Mol Med Rep*, vol. 9, no. 3, pp. 779–785, Mar. 2014, doi: 10.3892/MMR.2013.1875/HTML.

[87] R. A. Hess and C. M. K. Morrow, “Claudin 5, Germ Cells, and the Blood-Testis Barrier.,” *Biol Reprod*, vol. 83, no. Suppl_1, pp. 109–109, Nov. 2010, doi: 10.1093/BIOLREPROD/83.S1.109.

[88] J. H. C. Wang, “Cell Traction Forces (CTFs) and CTF Microscopy Applications in Musculoskeletal Research,” *Oper Tech Orthop*, vol. 20, no. 2, p. 106, Jun. 2010, doi: 10.1053/J.OTO.2009.10.007.

[89] U. S. Schwarz and J. R. D. Soiné, “Traction force microscopy on soft elastic substrates: A guide to recent computational advances,” *Biochimica et Biophysica Acta (BBA) - Molecular Cell Research*, vol. 1853, no. 11, pp. 3095–3104, Nov. 2015, doi: 10.1016/J.BBAMCR.2015.05.028.

[90] B. Srinivasan, A. R. Kolli, M. B. Esch, H. E. Abaci, M. L. Shuler, and J. J. Hickman, “TEER measurement techniques for in vitro barrier model systems,” *J Lab Autom*, vol. 20, no. 2, p. 107, Apr. 2015, doi: 10.1177/2211068214561025.

[91] K. Felix, S. Tobias, H. Jan, S. Nicolas, and M. Michael, “Measurements of transepithelial electrical resistance (TEER) are affected by junctional length in immature epithelial monolayers,” *Histochem Cell Biol*, vol. 156, no. 6, pp. 609–616, Dec. 2021, doi: 10.1007/S00418-021-02026-4/FIGURES/4.

[92] E. M. Shaughnessey, S. H. Kann, H. Azizgolshani, L. D. Black, J. L. Charest, and E. M. Vedula, "Evaluation of rapid transepithelial electrical resistance (TEER) measurement as a metric of kidney toxicity in a high-throughput microfluidic culture system," *Scientific Reports 2022 12:1*, vol. 12, no. 1, pp. 1–14, Aug. 2022, doi: 10.1038/s41598-022-16590-9.

[93] O. Livnah, E. A. Bayert, M. Wilchekt, and J. L. Sussman, "Three-dimensional structures of avidin and the avidin-biotin complex (deglycosylated avidin/divergent evolution/x-ray crystallography/streptavidin)," *Proc. Natl. Acad. Sci. USA*, vol. 90, pp. 5076–5080, 1993.

[94] T. N. Demidova-Rice, J. T. Durham, and I. M. Herman, "Wound Healing Angiogenesis: Innovations and Challenges in Acute and Chronic Wound Healing," *Adv Wound Care (New Rochelle)*, vol. 1, no. 1, p. 17, Feb. 2012, doi: 10.1089/WOUND.2011.0308.

[95] S. R. K. Vedula, A. Ravasio, C. T. Lim, and B. Ladou, "Collective cell migration: A mechanistic perspective," *Physiology*, vol. 28, no. 6, pp. 370–379, Nov. 2013, doi: 10.1152/PHYSIOL.00033.2013/ASSET/IMAGES/LARGE/PHY0061301800004.JPEG.

[96] R. Alert and X. Trepat, "Physical Models of Collective Cell Migration," *Annu Rev Condens Matter Phys*, vol. 11, pp. 77–101, Mar. 2020, doi: 10.1146/ANNUREV-CONMATPHYS-031218-013516.

[97] M. Zhao, H. Bai, E. Wang, J. V. Forrester, and C. D. McCaig, "Electrical stimulation directly induces pre-angiogenic responses in vascular endothelial cells by signaling through VEGF receptors," *J Cell Sci*, vol. 117, no. Pt 3, pp. 397–405, Jan. 2004, doi: 10.1242/JCS.00868.

[98] Z. Zhao *et al.*, “Optimization of Electrical Stimulation for Safe and Effective Guidance of Human Cells,” *Bioelectricity*, vol. 2, no. 4, pp. 372–381, Dec. 2020, doi: 10.1089/BIOE.2020.0019.

[99] D. J. Leaper, M. E. Foster, S. S. Brennan, and P. W. Davies, “An experimental study of the influence of magnetic fields on soft-tissue wound healing.,” *J Trauma*, vol. 25, no. 11, pp. 1083–1084, Nov. 1985, Accessed: Jul. 26, 2022. [Online]. Available: https://europepmc.org/article/med/3903177

[100] “Arduino Waveform Generator : 5 Steps (with Pictures) - Instructables.” https://www.instructables.com/Arduino-Waveform-Generator-1/ (accessed Mar. 19, 2023).